Volume 4
Number 19
7 October 2023
Pages 4261–4622

Materials Advances

rsc.li/materials-advances

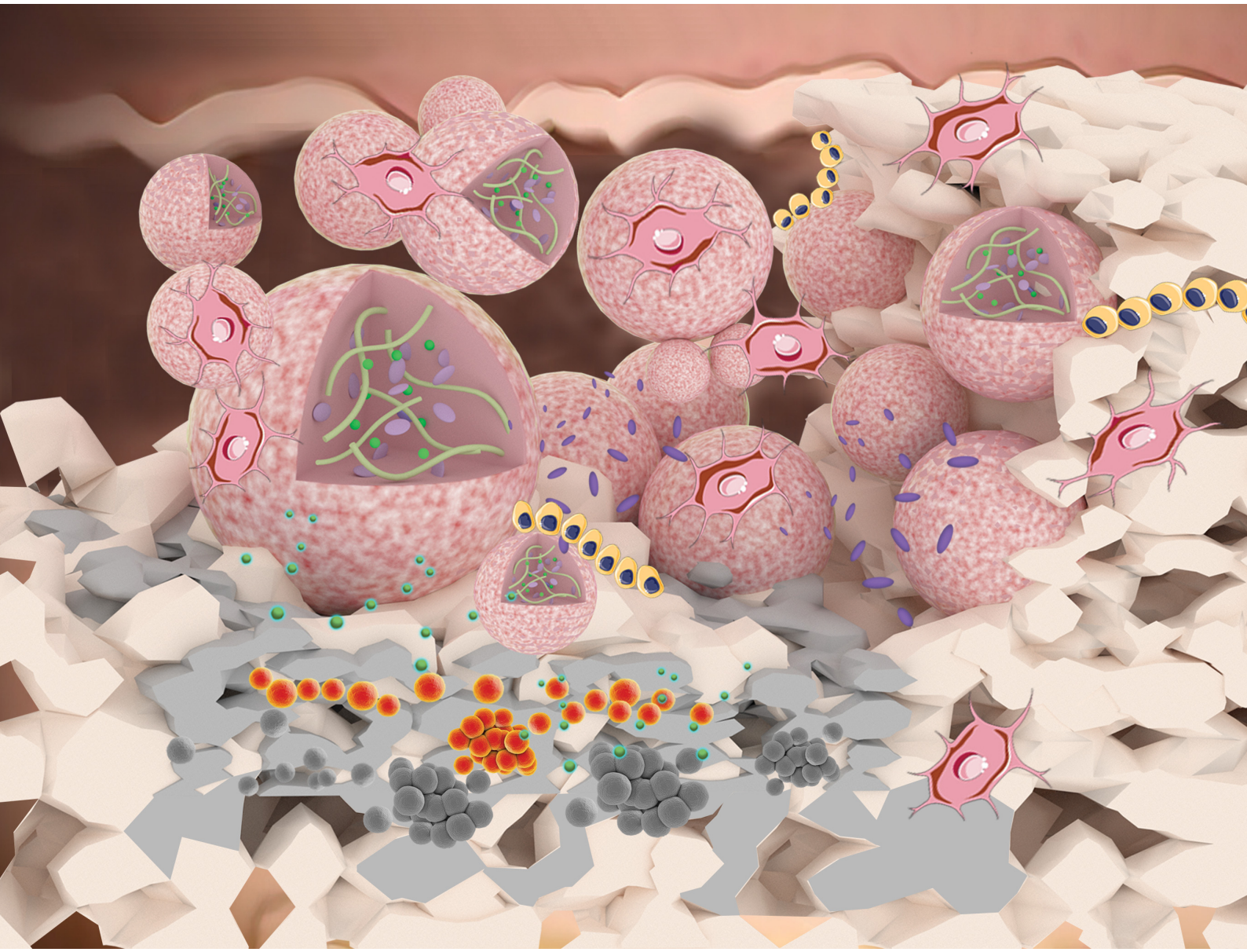

ISSN 2633-5409

ROYAL SOCIETY OF CHEMISTRY

PAPER
Yubao Li, Qin Zou *et al.*
Injectable gelatin microspheres for osteomyelitis treatment: osteogenic and anti-inflammatory effect

Materials Advances

ROYAL SOCIETY OF CHEMISTRY

PAPER

View Article Online
View Journal | View Issue

Cite this: *Mater. Adv.*, 2023, 4, 4349

Injectable gelatin microspheres for osteomyelitis treatment: osteogenic and anti-inflammatory effect

Rui Zhang,[a] Li Chen,[b] Yijing Stehle,[c] Mingyue Lin,[a] Chenxin Wang,[a] Yufan Li,[a] Min Huang,[d] Yubao Li*[a] and Qin Zou *[a]

The clinical treatment of osteomyelitis usually involves surgical debridement, necrotic bone removal, and subsequent biomaterial transplantation to fill the void. The transplanted biomaterials need to be able to fight the pathogens invading the infection after trauma, orthopedic surgery or joint replacement and be able to relay regenerative events. Here, injectable vancomycin (Van)-loaded gelatin/nanohydroxyapatite (Gel/n-HA) composite microspheres (VM) with both antibacterial and bone regenerative properties were prepared for osteomyelitis treatment. The impact of Gel/n-HA-injectable composite microspheres (M) on cell recruitment, proliferation, and osteogenic differentiation was evaluated. Osteoblasts were successfully recruited by M to the bone defect area *in vivo*. Furthermore, the release kinetics of Van from VM *in vitro* and anti-inflammatory activity *in vivo* were assessed as the efficacy of the released antibiotics, which inhibited cell wall synthesis in *Staphylococcus aureus*, thereby lysing the bacterial cells. When administered topically to rabbit tibia osteomyelitis defects, the injectable VM enhanced *in vivo* bone healing and fracture resistance. Thus, owing to the injectability and coordinated therapeutic actions of VM, they are considered promising biomaterials with osteogenic and anti-inflammatory potential for osteomyelitis treatment.

Received 3rd June 2023,
Accepted 23rd July 2023

DOI: 10.1039/d3ma00279a

rsc.li/materials-advances

1. Introduction

Osteomyelitis occurs because of microbial invasion or autoinflammatory processes and can drastically compromise the functionality and regenerative capacity of osseous tissues.[1] Gram-positive Staphylococci constitute the most common pathogen of osteomyelitis (~75%) and can cause bone destruction at the infection site by inducing osteoblast apoptosis,[2] activating osteoclast formation, and secreting toxins.[3] Sequestrum formation following infection produces bone defects not conducive to local infection control, with hematoma formation in these defects creating opportunities for bacterial colonization.[4] In the later stages of osteomyelitis, dead bone almost fully covers the original living bone. Ischemia can potentially induce bone necrosis by obliterating the bone vascular channels, thereby reducing blood supply.[5] The separation of ischemic bone segments forms sequestra. Consequently, an avascular area inaccessible to antibiotics and inflammatory cells is formed that provides a suitable environment for continued bacterial growth.[6] The first task in the treatment of osteomyelitis is to clear the bacterial infection. Systemic antibiotic application can help reduce infection; however, the local ischemic condition and the presence of the "blood–bone" barrier cause poor antibiotic penetration at the site of interest.[7] Clinical treatment usually includes surgical debridement, necrotic bone removal, and subsequent autologous bone transplantation to fill the void.

Therefore, numerous bone implantable biomaterials, such as microspheres, have been developed with antibiotics[8,9] (*i.e.*, gentamicin sulfate,[10] ibuprofen,[11] or lysozyme[12]) incorporated for administration to localized defective sites to protect against bacterial infection while simultaneously enabling bone repair.[13] Spherical microspheres have versatile applications either as suspensions or (colloidal) gels that can be applied using minimally invasive surgery.[14] The microsphere-type scaffold is easily applied *via* syringe needle injection into the bone defect sites for repairing irregular and complex defects. Gelatin is derived from collagen by breaking down the triple-helical structure of collagen. Gelatin contains the sequence of arginine–glycine–aspartic acid (RGD) which is the specific recognition site of integrins and is involved in regulating the

[a] *Research Center for Nano Biomaterials, Analytical & Testing Center, Sichuan University, Chengdu 610064, P. R. China. E-mail: nic7504@scu.edu.cn, zouqin80913@126.com*
[b] *Analytical & Testing Center, Sichuan University, Chengdu 610064, P. R. China*
[c] *Department of Mechanical Engineering, Union College, 807 Union St., Schenectady, NY 12308, USA*
[d] *Sichuan Institute of Atomic Energy, Chengdu, 610101, P. R. China*

interactions between cells and the extracellular matrix.[15] Incorporation of nanohydroxyapatite (n-HA) into gelatin was shown to generate composite microspheres with increased hydrophilicity and osteoconductivity. With the increase of n-HA content, the protein adsorption capacity of the composite microspheres significantly increased.[16] The architecture of n-HA can offer biophysical information for the adjustment of cell behaviors (*e.g.*, cell attachment, spreading, proliferation, or differentiation) and the subsequent process of osteogenesis for bone regeneration.[17] Previously, we reported the preparation of gelatin/nanohydroxyapatite (Gel/n-HA) (10 wt%) composite microspheres using a water-in-oil emulsification process and subsequent crosslinking with 1-ethyl-3-(3-dimethylaminopropyl)carbodiimide (EDC).[18] These microspheres exhibited superior cytocompatibility as they possessed sustainable regenerative effects for bone healing with the zero-length crosslinking agent (EDC) and are entirely degradable. Studies have shown that drug and biomolecules can be readily loaded into gelatin microspheres *via* diffusion, which avoids the contact with harsh organic substances during the crosslinking reaction.[19] Vancomycin (Van) is a glycopeptide antibiotic that inhibits bacterial cell wall synthesis through a five-hydrogen bond interaction between the heptapeptide backbone of the antibiotic and the C-terminal D-alanyl–D-alanine (D-Ala–D-Ala) dipeptide, consequently lysing the bacterial cell walls and causing cell death.[20] A nanocomposite fibrous scaffold (silica-coated n-HA-gelatin reinforced with poly(L-lactic acid) yarns) containing Van for treating osteomyelitis in a rat model was shown to be highly efficacious.[21] In recent years, bone tissue regeneration through endogenous stem cell "homing" and recruitment has received more attention.[22] It utilizes the body's own regeneration capacity to repair bone tissue while avoiding exogenous cell-associated limitations. The appropriate selection of cell-adhesion signaling molecules and the identification of a suitable linking strategy that ensures efficient and reliable mobilization of the selected adhesion signaling molecules

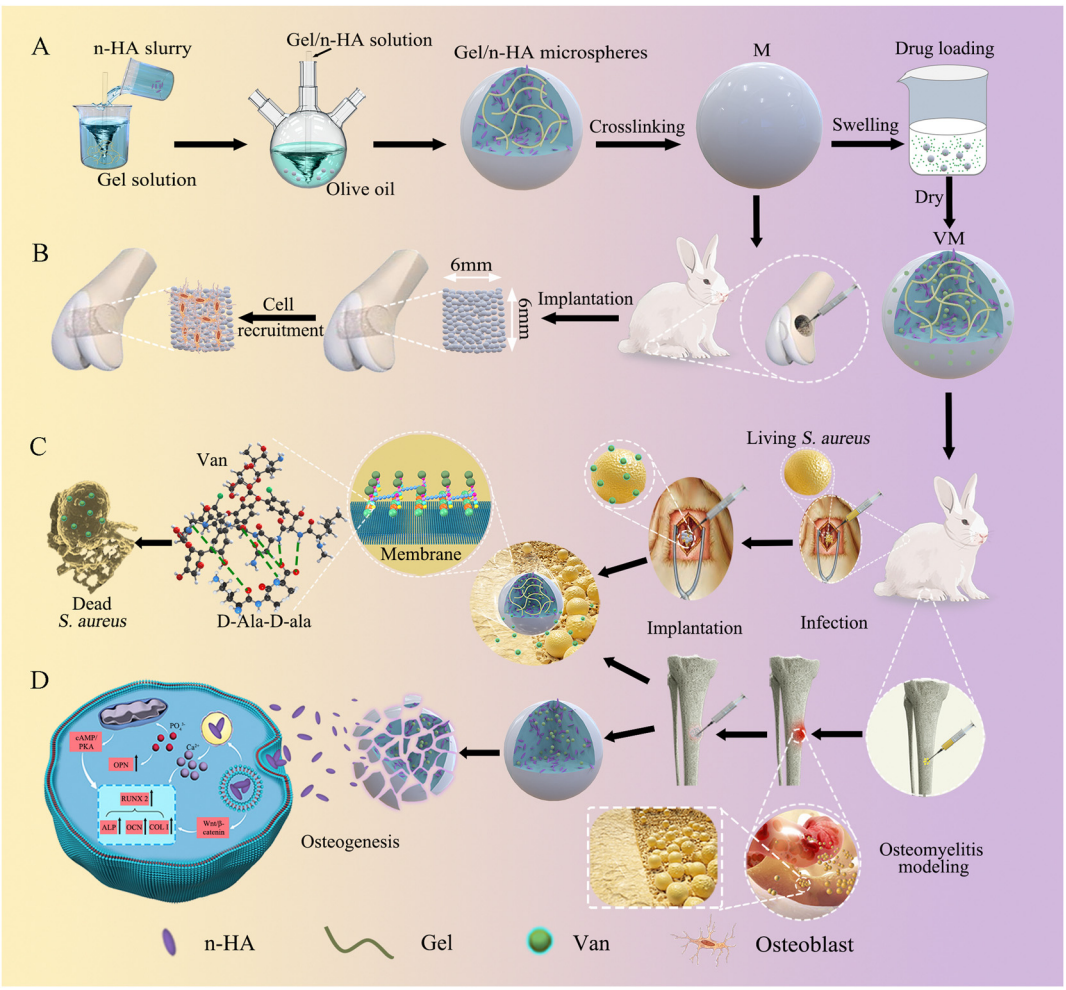

Scheme 1 Schematic illustration of the preparation of vancomycin-loaded microspheres (VM) for osteomyelitis treatment. (A) Preparation of gelatin/nanohydroxyapatite composite microspheres (M) and VM; (B) illustration of the bone regeneration promotion of M in a rabbit femoral condyle model; (C) anti-infection mechanism of VM in the back muscles; and (D) illustration of the antibacterial and osteogenic mechanisms of VM in an osteomyelitis model. n-HA, nanohydroxyapatite; Gel, gelatin; Van, vancomycin.

while preserving their biochemical functions are key considerations when designing cell instructive biomaterials.[23] Many strategies, such as native ECM proteins and protein fragments of gelatin, are popular choices for promoting the adhesion of stem cells to the surfaces of biomaterials, regulating immune cell infiltration and reducing the inflammatory effects of biomaterials.[24] Ke *et al.* described the production of a 3D gelatin microsphere scaffold with multiple voids designed and manufactured on the basis of facile fabrication of gelatin microspheres. The effective production of this scaffold can be used to promote tissue migration and nerve recovery after spinal cord injury.[25] Limited stem cell sources restrict the *ex vivo* expansion of exogenous stem cells and *in vivo* delivery of growth factors for osteomyelitis treatment. Hence, the most effective and feasible strategy to apply this treatment is by exploiting injectable scaffolds loaded with targeted antibacterials against local infection and cell recruitment activities reflecting the osteogenic cell niche that can interact with the surrounding host tissue to achieve rapid homeostasis by recruiting embryonic stem cells and promoting angiogenesis and osteogenesis.[26]

Here, we exploited the water-in-oil emulsification method to fabricate Gel/n-HA-injectable composite Van-loaded microspheres (VM) as a local delivery system (Scheme 1). We aimed to examine whether the targeted antibacterial and cell recruitment activities *in vitro* of VM translate to an effective osteomyelitis treatment. Further, we tested the hypothesis that EDC crosslinked microspheres support osteogenesis. Microsphere degradation and bone formation supported by the microscaffolds in the femoral condyle defect group were monitored using microcomputed tomography (Micro-CT) and histology. We validated the feasibility of Van delivery for antibacterial activity *via* VM. The drug release kinetics and antibacterial mechanism of VM were assessed using the drug release profile and scanning electron microscopy (SEM), transmission electron microscopy (TEM), and live/dead staining of bacteria. Finally, a rabbit model of osteomyelitis was employed to assess the overall hypothesis of the targeted antibacterial, inflammation modulatory, osteoblast recruitment, and bone regenerative properties of VM *in vivo*. The inflammation modulatory effect, particularly in killing bacteria, and the morphology of bone formation in the osteomyelitis model following treatment were evaluated using end-point histology and sequence fluorescent labeling.

2. Materials and methods

2.1 Materials and reagents

Gel type A was purchased from Sigma-Aldrich, USA. n-HA slurry was synthesized by a wet chemical method in our laboratory.[27] All chemical reagents obtained from commercial routes were of analytical grade and were used without further purification.

2.2 Preparation of microspheres

The injectable Gel/n-HA microspheres (M) were prepared by a water-in-oil emulsion method.[18] Briefly, Gel (1.5 g) was completely dissolved in distilled water (10 mL) at 40 °C to form a homogeneous aqueous Gel solution before the addition of n-HA slurry (30 w/v%, Gel : n-HA = 9 : 1). Next, the solution was poured into olive oil in a three-neck round-bottom flask and further stirred with an upper stirrer for 15 min (400 rpm) followed by chilling to below 10 °C for 30 min. To form this W/O emulsion, acetone (100 mL) was added to the suspension mixture and stirred for 15 min. The microspheres were separated by centrifugation at 4 °C, and fully washed with acetone to remove oil. Finally, the microspheres (dried at 45 °C for 12 h in an oven in air) were crosslinked in EDC/acetone aqueous solution (0.1%, w/v) at room temperature for 12 h.

The swellable properties of the drug carrier loaded Van in the M have been reported.[28] Briefly, the Van was loaded allowing the microspheres (1 g) to swell at 37 ± 0.2 °C under continuous magnetic stirring (120 rpm) in a water solution of Van (1 g/125 mL) for 6 h. The resulting Van-loaded Gel/n-HA composite microspheres (VM) were finally washed 3 times with ethanol by centrifiltration and lyophilization.

2.3 Characterization of microspheres

The particle size distribution of M and VM was measured by laser diffractometry (laser particle size analyzer, Mastersizer 2000, Malvern, UK). Scanning electron microscopy (SEM, Apreo S, Thermo Scientific, USA) was used to observe the surface of M and VM and observe the cross-section of M and VM which were embedded in the glycol methacrylate monomer[29] (Technovit®7200 VLC, Germany). Energy-dispersive X-ray spectroscopy (EDS, X-MaxN 80, Oxford, UK) was used for elemental analysis. The phase composition and crystallinity of samples were analyzed by X-ray diffraction (XRD, PANalytical B.V, EMPYREAN, Netherlands). The infrared spectra of samples were collected by Fourier transform infrared spectrometry (FT-IR, Invenio R, BRUKER, Germany). The M and VM filled in bones were scanned by microcomputed tomography (Micro-CT, Viva CT80, SCANCO Medical AG, Switzerland).

2.4 Biocompatibility and osteogenic differentiation of M

2.4.1 Cell proliferation assay of MG63 *in vitro*. To evaluate the cell adhesion and proliferation of the M, the human osteosarcoma MG63 cells (a non-transformed cell line that exhibits an osteoblastic phenotype) cultured in F-12 nutrient mixture medium (Gibco, Life Technologies, USA) containing 10% newborn calf serum (NBCS, Gibco, Life Technologies, USA) and 1% penicillin–streptomycin antibiotic solution (MP Biomedicals, USA) were seeded on the M at a seeding density of 1.6×10^4 cells per well followed by incubation at 37 °C with 5% CO_2. After incubating for 4 days, the cell/microsphere samples were observed by SEM. Cell attachment, spreading, and morphology were assessed by fluorescent staining of actin (Alexa Flour® 532 phalloidin, Invitrogen), mitochondria (mitochondria-selective probes, Mito Tracker® probes, Invitrogen), and nuclei (Hoechst dyes, Invitrogen). The samples were visualized using a confocal laser scanning microscope (CLSM, A1R MP +, Nikon). The cells were labeled with a live/dead reagent (a viability/cytotoxicity kit, Life Technologies, USA) after

culture for 7 days and the morphology of cells was imaged by using an inverted fluorescence microscope (Ti-U, Nikon, Japan) to reveal the cell viability on M.

2.4.2 Osteogenesis analysis of BMSCs *in vitro*. Bone marrow stromal cells (BMSCs) were isolated from 100 g of healthy SD rats. After euthanasia, femurs were detached under sterile conditions, and BMSCs were harvested from the metaphysis of both ends. Then, cells were cultured in α-modified Eagle's medium (α-MEM; Gibco, Life Technologies, USA) containing 10% NBCS and 1% penicillin–streptomycin antibiotic solution. The cells were incubated in a humidified atmosphere of 5% CO_2 and 95% air at 37 °C, and the culture medium was changed every two days. Cells were subcultured when they grew to 80% of the bottom of the cell culture flask. BMSCs at a density of 2×10^4 cells per mL were seeded on the M for 14 days and the cells were harvested and fixed in 2.5% paraformaldehyde at 4 °C overnight. Then, the cells were dehydrated stepwise in ethanol and embedded in epoxy resin. The fixed samples were cut into ultrathin sections using an Ultracut ultramicrotome (Leica, Germany) and lightly stained with 1% uranyl acetate and lead citrate for transmission electron microscopy (TEM, G2F20S-TWIN, USA) observation.

For the quantitative real-time polymerase chain reaction (qPCR) assay,[30,31] after BMSCs were seeded on the M at 5×10^4 cells per mL for 7 and 14 days, total RNAs of BMSCs were extracted and collected by using the Trizol reagent (Life Technologies), the quantity of RNA was detected by the OD value, and the integrity of RNA was determined by 1% agarose gel electrophoresis. The first-strand cDNA was synthesized using the Super-Script First-Strand Synthesis System (Gene seed), followed by the amplification of the cDNA product using Platinum Taq DNA polymerase (Gene seed). The first-strand complementary DNA (cDNA) was synthesized by using the reaction fluid (4 μL of 5 × RT buffer, 2 μL of geneseed® enzyme mix, 1 μL of reverse transcription primer, 1 μg of total RNA, and 20 μL of RNase free ddH_2O) at 25 °C for 10 min, 42 °C for 60 min, and 85 °C for 5 min, respectively. β-Actin was considered as the internal control gene in this analysis. The primer sequences of the genes are summarized in Table 1.

The qPCR reaction system was prepared using 10 μL of 2 × SYBR Green PCR Master Mix, 0.4 μL of forward primer, 0.4 μL of reverse primer, and 20 μL of ddH_2O. The PCR initiated denaturation at 95 °C for 5 min. Then 40 cyclic reactions were carried out, each of which was composed of denaturation at 95 °C for 10 s and acquisition signals at 60 °C for 34 s. Eventually, the dissolution was reacted at 95 °C for 15 s, 60 °C for 60 s, and 95 °C for 15 s. Reaction specificity was confirmed by analyzing the melting curves of the products and the electrophoresis of the products on a 1.0% agarose gel. The relative changes in gene expression were analyzed *via* the 2(−Delta Delta C(T)) method and normalized according to the expression of the housekeeping gene β-actin.

2.4.3 Degradation and osteogenesis of M *in vivo*. New Zealand white rabbits (2–3 kg) were obtained from the Sichuan University Laboratory Animal Center. All the experiments were approved by the Ethics Committee of Sichuan University. A total of 24 skeletally mature New Zealand White rabbits were randomly assigned to 5 groups for 10, 16, 28, or 56 days implantation of ethylene oxide sterilized M and the blank control, respectively. M was inserted into the bone defect (Φ 6 mm × 6 mm) created in the medial femoral condyle.[32] The incision was sutured layer upon layer. After surgery, each rabbit was intramuscularly injected with penicillin (1×10^5 units per day) which lasted for 3 days. 10, 16, 28, or 56 days after implantation, three femur samples with implants in each group were harvested and the immobilized (in 4% buffered paraformaldehyde) samples were scanned using microcomputed tomography (Micro-CT, Viva CT80, SCANCO Medical AG, Switzerland). Based on the original CT scans of each sample, three-dimensional images were reconstructed. The quantitative evaluation of osteogenesis such as bone volume/total volume (BV/TV) and bone mineral density (BMD) was done based on the SCANO MEDICAL μCT Evaluation Program software. A cylindrical region of interest (ROI with the same size as the bone defect) was selected to characterize the degradation of M and characterize the new bone formation inside the bone defect. Samples for histological analysis were embedded in paraffin. After cutting, the sections were stained with hematoxylin and eosin (HE) and Masson, and finally observed by using a stereoscope (SMZ800N, Nikon, Japan) and a microscope (Ti-U, Nikon, Japan).

2.5 Antibacterial ability and release evaluation of Van of the VM

2.5.1 Bacteria cultured with VM *in vitro*. The morphologies of bacteria treated with samples (M, VM) were observed by SEM. The samples (5 mg) were sterilized with ethylene oxide and transferred to a 24 well plate. Then, 200 μL of bacterial solution containing 1×10^7–10^8 CFU mL^{-1} *Staphylococcus aureus* (*S. aureus*, CMCC26003) and *Escherichia coli* (*E. coli*, CMCC(B)44102) was dripped separately. After incubating for 24 h, the bacteria were immobilized with 2.5% (v/v)

Table 1 Primers designed for selected genes in relation to osteogenic differentiation of BMSCs

mRNA	Forward primer	Reverse primer
β-actin	GGCCGGGACCTGACAGACTACCTC	GTCACGCACGATTTCCTTCTCAGC
COL 1	ACGGCTGCACGAGTCACAC	GATGGGOAGGCGGGAGGTCITG
RLNX 2	GCCQTAGAGAGCAGGGAAGAC	CTGGCTTGGATTAGGGAGTCAC
ALP	CGGGCAGTGTGACGGTAAATA	ACATCGGGGGCAGGCAGACT
OCN	ACCGGGAGCAGTGTGAGC	GATGCGTTTGTAGGCGGTCTTC
OPN	TGGCTGAATTCTGAGGGACTAACT	ACTTTCACCGGGAGGGAGGAG

paraformaldehyde and dehydrated gradually with gradient ethanol (20, 40, 60, 80, and 100% v/v) for 10 min. After freeze-drying, the bacteria on the surface of the samples were observed by SEM. In addition, bacterial cells were also analyzed by TEM.[33] After the mixture of bacteria and samples cocultured for 24 hours was centrifuged (1000 r min^{-1}, 5 min), the supernatant was discarded, and 2.5% glutaraldehyde was added to fix the samples for 2 hours. The samples were dehydrated stepwise in ethanol and embedded in epoxy resin. The fixed samples were cut into ultrathin sections using an Ultracut ultramicrotome and were lightly stained with 1% uranyl acetate and lead citrate for TEM. Live/dead staining was used to visually observe the live/dead states of bacteria. The bacteria (1×10^8 CFU mL^{-1}) blended with samples (5 mg) were cocultured for 24 h. After that, the bacteria after different treatments were stained with SYTO9 and PI (LIVE/DEAD bacterial viability kit, Thermofisher) for 15 min. Finally, photographs were taken under a fluorescence microscope. Living bacteria appear green, and dead bacteria appear red. The intensity of fluorescent staining was semi-quantitatively analyzed by Image J software.[34]

2.5.2 Release evaluation of Van from VM. The antibiotic concentration and encapsulation effectiveness were determined by dissolving 1 g of VM completely in 4 mL of PBS (pH 7.4), centrifuging the supernatant, and measuring the absorbance at 280 nm using ultraviolet-visible (UV) spectroscopy (UV-Vis V-2401, Japan). The three average values were used to quantify the antibiotic content and encapsulation effectiveness using a calibration curve that was created using the known vancomycin concentration. To evaluate the release characteristics of VM, the microspheres (200 mg, $n = 4$) were dispersed in a dialysis bag (8000 Da) containing 5 mL of PBS with pH 7.4 or pH 6.0 and then immersed in brown sample bottles containing 10 mL of release medium (pH 7.4 or pH 6.0). All the samples were placed in a constant temperature shaker (37 °C, 120 rpm min^{-1}). At designated time intervals (0.5 h, 1 h, 2 h……14 d), 4 mL of the solution was taken out for analysis and replaced with the same volume of fresh solution to ensure a constant volume. According to the maximum absorption wavelength of the full spectrum of UV absorption of Van solution (280 nm),[35] the content of Van was detected at 280 nm by UV spectroscopy. The VM cumulative release ratio (%) was calculated using eqn (1):[36]

$$\text{Cumulative release percentage}\,(\%) = \sum_{t=0}^{t} \frac{M_t}{M_0} \times 100 \qquad (1)$$

where M_t is the cumulative amount of Van released at each sampling time point, t is the time of the release, and M_0 is the initial weight of the Van loaded in the sample.

The KB disk diffusion method was used to evaluate the bioactivity of the Van released under different pH conditions. The bacterial zone of inhibition (killed bacteria) is related to the quantity and efficacy of the released antibiotic. For this, about 30 μL of the released Van at different time points (0–14 days) was added to a 6 mm sterile filter-paper disk and then air-dried. *S. aureus* (1 mL, 10^8 CFU mL^{-1}) was seeded on the prepared agar plate and the prepared filter paper samples were placed on the agar plate. The zones of inhibition were measured after 24 h incubation at 37 °C.

2.5.3 Treatment of infected wound of back muscle *in vivo*. In order to evaluate the antibacterial effect of VM *in vivo*, a rabbit back muscle *S. aureus* infection model was established.[37] New Zealand white rabbits, weighing 2–3 kg, were anesthetized by intravenous administration of 3% (w/w, 30 mg kg^{-1}) pentobarbital sodium. The muscular incision of approximately 10 mm on the back of rabbits was exposed under aseptic conditions. The rabbit muscle without infection was set as control. The other rabbits' back muscles were then infected with 50 μL of *S. aureus* (1×10^8 CFU mL^{-1}). After infection, the samples were divided into 4 groups: an infected group that did not receive any treatment as blank; Van group that received a single treatment with Van; and another two groups that were injected M (100 mg) and VM (100 mg) at the same dosage as the single Van treated group, respectively. On the fourth day, all the rabbits were sacrificed and photographed and the tissues at the wound site were sliced, followed by H&E staining. According to the method of Jia *et al.*,[38] a sterile cotton swab was used to collect the mucus from the infected area and then transfer it into a centrifuge tube containing 10 mL of sterile physiological saline. Serial dilutions of the bacterial suspension (10^{-1}, 10^{-2}, 10^{-3}, …10^{-7}) were made, and finally a pipette gun was used to transfer 50 μL of each dilution onto the solid medium and spread well. The plates were incubated in an incubator at 37 °C for 24 h and then counted. Plates with three parallel groups of three per dilution and colonies in the range of 30–300 were considered valid.

2.6 Treatment of rabbit osteomyelitis

Next, we developed an animal model with induced infection to evaluate its potential as a promising adjuvant therapy for osteomyelitis (Fig. 1A). The rabbit tibia osteomyelitis model was established according to the literature.[39–41] All surgical procedures were approved and performed by the Ethics Committee of West China Hospital at Sichuan University. Ten adult pathogen-free New Zealand white rabbits (~3.0 kg per each) were anesthetized with 3% (w/w, 30 mg kg^{-1}) pentobarbital sodium. After anesthesia, the hair was removed from the hind legs and the skin was disinfected. A skin incision was made in the medial tibia of the rabbits. The skin and musculature were dissected and the tibia was exposed (Fig. $1B_1$). A bone defect model (2 mm in diameter, deep into the medullary cavity) was created on the medial side of the anterior tibia using a drill. Two longitudinally connected and partially overlapped bone holes were drilled here to reach the medullary cavity to make a rectangular bone window (Fig. $1B_2$). Osteomyelitis was induced by injecting 0.1 mL of *S. aureus* suspension (1×10^8 CFU mL^{-1}) and 0.1 mL of 5% sodium morrhuate (Xinyi Pharmaceutical, China) into the tibia of the rabbits (Fig. $1B_3$). After sealing the bone window with bone wax and washing the wound with normal saline, the musculature and the skin were closed with sutures separately. After 6 weeks, the rabbits were sacrificed to

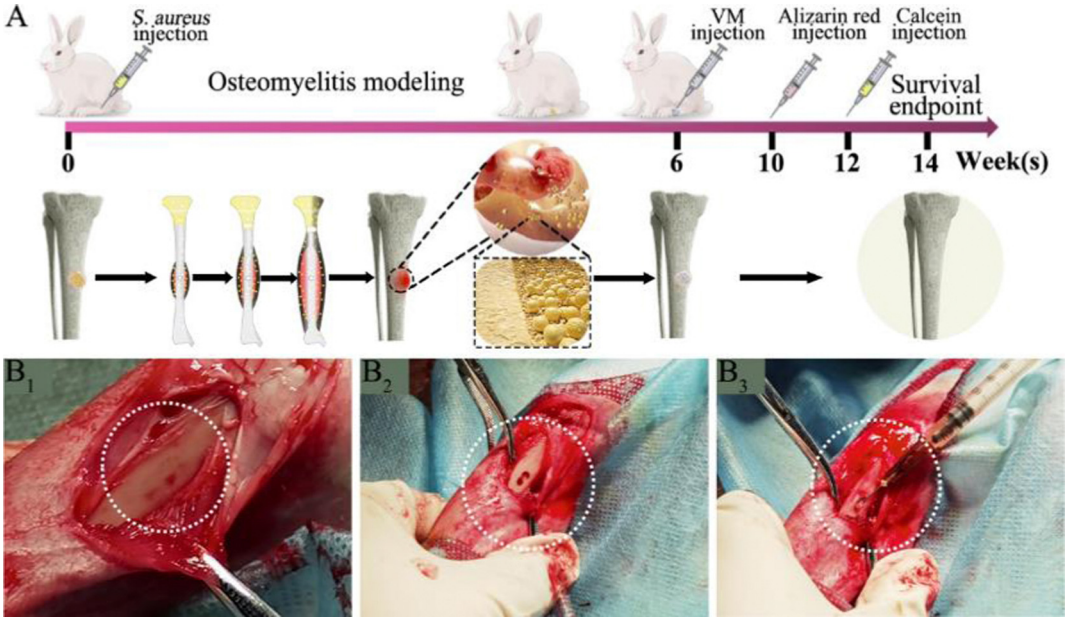

Fig. 1 Schematic diagram of rabbit osteomyelitis modeling and treatment. (A) Schedule of rabbit osteomyelitis surgery. (B) Surgical procedure for osteomyelitis: (B_1) blunt dissection of subcutaneous muscle; (B_2) creation of bone defects; (B_3) injection of *S. aureus*.

confirm the presence of osteomyelitis through microbiological and X-ray imaging, according to the method described by Norden *et al.*[40]

Six weeks following surgery, a yellow viscous purulent liquid and granular purulent tissue can be seen around the site of the previous operation and a large number of bacterial colonies can be observed after incubation of the purulent liquid (Fig. $2A_1$ and A_2). Obvious bone abscesses can be found by exposing the tibia (Fig. $2A_3$). Radiographic features (Fig. $2A_4$) of osteomyelitis including osteoporosis, peripheral osteosclerosis, cortical bone thinning, and bone destruction were observed in osteomyelitis modeling. SEM examination (Fig. $2A_5$) revealed the presence of *S. aureus* clusters within the biofilm on the implant surface, densely packed within a thin necrosed bone. Under strictly sterile conditions, after subcutaneous abscess removal, the loose and necrotic bone and soft tissue were delicately debrided in the area of osteomyelitis infection (Fig. $2B_1$). For different treatments, Van solution was used to wash the infected site repeatedly in the control group and the VM group was washed with Van solution and injected with VM into the intramedullary canal (Fig. $2B_2$ and B_3). Finally, the bone defect was sealed by bone wax, and then the wounds were sutured.

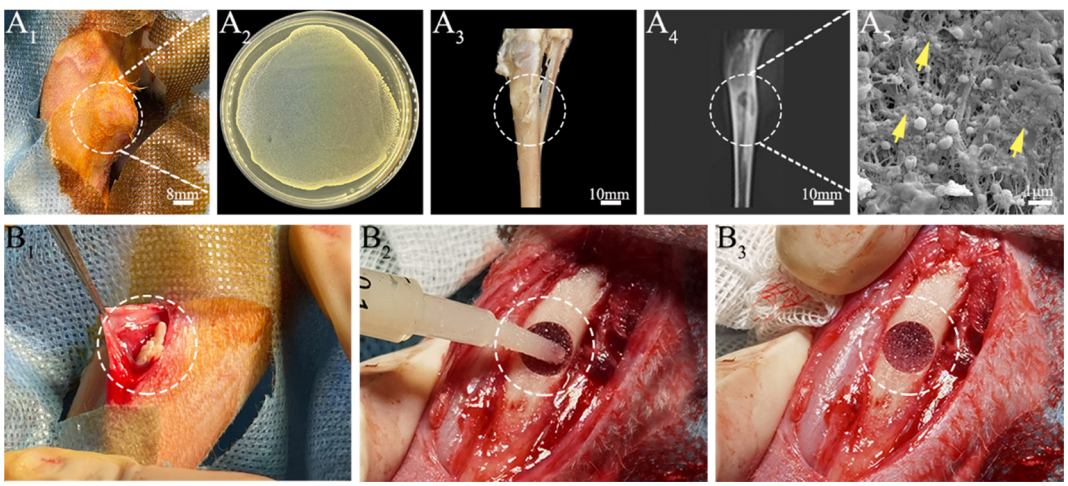

Fig. 2 Evaluation and treatment of the rabbit osteomyelitis model. (A_1) Gross observation around osteomyelitis modeling; (A_2) Identification of the pus near osteomyelitis infection: morphology of pus samples after culturing on the agar plate; (A_3) General photos, (A_4) X-ray radiographs of osteomyelitis modeling tibia, and (A_5) SEM images of *S. aureus* adhered on the bone infection area (white circle: osteomyelitis modeling area, yellow arrow: *S. aureus* biofilm). (B_1) surgical debridement of infectious tissue; (B_2) implantation of microspheres into the bone defects; (B_3) Implanted microspheres.

The sequence fluorescent labeling investigation was conducted to detect the rate of new bone formation and mineralization.[42,43] Briefly, after VM implantation for 4 weeks, the animals were subjected to intramuscular injection of 30 mg kg^{-1} Alizarin red solution (Sigma, USA). Besides, additional calcein solution at a dose of 20 mg kg^{-1} (Sigma, USA) was also injected two weeks before sacrifice. At 8 weeks, the rabbits were sacrificed and the tibias were harvested. Fresh bone tissues were fixed in 4% buffered paraformaldehyde, embedded in resin and sliced. The cut sections stained by HE were observed by using a microscope. The other sections without staining were then imaged by CLSM.

8 weeks after the microsphere treatment, all animals were sacrificed and the tibias were harvested. The immobilized (in 4% buffered paraformaldehyde) samples were scanned using Micro-CT. Based on the original CT scans of each sample, three-dimensional images were reconstructed. The micro-morphological bone evaluation parameters include BMD and BV/TV. Samples for histological analysis were decalcified in 10% EDTA decalcifying solution for 2 months, then embedded in resin and cut into 5 μm sections after washing, dehydration, and wax immersion. Finally, the cut sections were stained by HE and Masson staining and then observed by using a microscope to analyze histopathological characteristics.

2.7 Statistical analysis

All the data were expressed as means ± standard deviations (SDs). One-way analysis of variance (ANOVA) was used to determine the statistical significance among different groups. When the p-value was <0.05, the statistics was considered significant, and $p < 0.01$ was considered remarkably significant.

3. Results

3.1 Characterization of M and VM

The particle sizes of M range between 8.7 and 51.8 μm (D50 = 31.1 μm) and those of VM range from 8.8 to 53.8 μm (D10 and D90, respectively), with a median size of 27.4 μm (D50) (Fig. 3A). Gel/n-HA composite microspheres (M) showed a very smooth spherical appearance with a few microwrinkles on the surface (Fig. 3B(top, left)). Both calcium (red) and phosphorus (green) elements were evenly distributed on the microsphere. The Van-loaded M (VM) sample was comprised of some miniscule particles compared to the unloaded microsphere. The large pores on the sphere interior and chloride elements (blue dots) on the surface and inside of the VM (Fig. 3B) were formed during the drug loading. The broad XRD diffraction peak of Gel and Van powder was located around 22° and 21°, respectively,

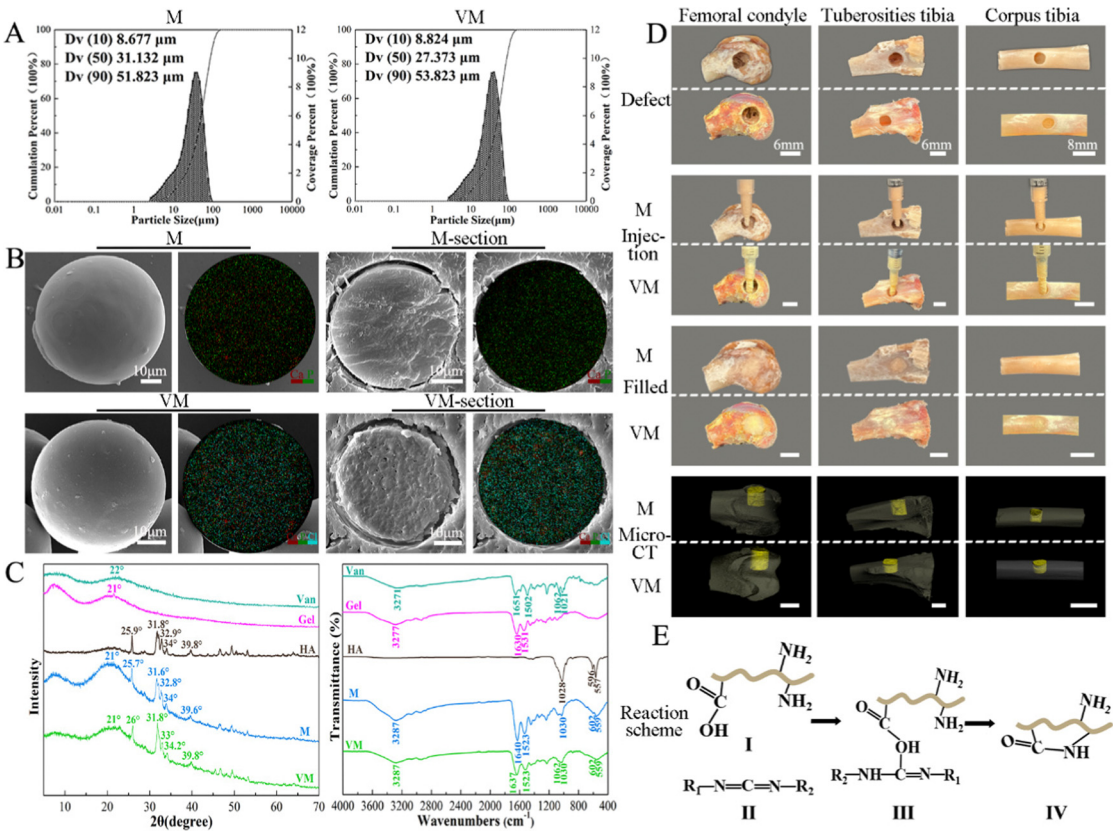

Fig. 3 Physicochemical properties of microspheres. (A) Particle size distribution curve of M and VM, (B) SEM (left) and EDS elemental map (right) of Ca/P/Cl of M and VM, (C) XRD patterns (left) and IR spectra (right) of Van, Gel, HA, M, and VM, (D) digital photos and 3D Micro-CT reconstructed images of bone defects, M and VM injection and filling of the femoral condyle, tuberosity tibia, and corpus tibia, (E) crosslinking reaction of Gel with EDC.

which proves the amorphous structure of Gel and Van. The diffraction peaks at 24.7°, 31.6°, 32.8°, 34°, and 39.6° (JCPDS#09-0432) indicated the presence of n-HA in M.[44] No apparent changes in the crystalline structure during the EDC crosslinking can be identified in the XRD spectral comparison. The addition of Van did not alter the crystallinity of the M or form new bonding according to Fig. 3C. According to IR spectra, the phosphate bands at 1030, 602, and 559 cm^{-1} which arise from the phosphate asymmetric bending vibrations slightly shift after crosslinking with EDC. The C═O absorption peak of the amide I band shifted from 1630 to 1640 $cm^{-1}$and that of the amide A band shifted from 3277 to 3287 cm^{-1}.45 VM exhibited a specific band at 1062 cm^{-1} corresponding to the stretching bending of C–O for Van (Fig. 3C).[46] Following the implantation of M and VM into the rabbit bone defect *ex vivo* model, a random stacking of both M and VM effectively filled the defect site completely, which demonstrated good injectability and plasticity and potential as an ideal injectable bone-filling material (Fig. 3D).[47]

3.2 Biocompatibility of M and associated effects on osteogenic differentiation of BMSCs

When MG63 cells were in close proximity with randomly distributed M, the cells explored their environment by extending filopodia and spikes, with numerous long multiple filopodia extending from the cell bodies connecting to distant M, leading to bridging (Fig. $4A_1$, black arrow). High-resolution imaging (Fig. $4A_2$) revealed that the MG63 cells were attached to the surface of M *via* pseudopodia to form tight, compact layers till the surface was well-coated. In the live/dead staining assay (Fig. 4B), numerous live cells (Fig. $4B_1$, green fluorescence) and a few dead cells (Fig. $4B_2$, red fluorescence) were observed, revealing that coated cells exhibited high viability and sufficient maturity to jointly form a layered film around the agglomerated M. Confocal microscopy staining was used to visualize the migration and proliferation of the cells that coated the three-dimensional (4C) structure of M. Diffuse and brightly stained nuclei (Fig. $4C_1$, blue) were observed on and around the M. Strong mitochondrial staining (green) indicated potential cell viability and proliferation on M (Fig. $4C_2$). The cells exhibited a fusiform and spreading morphology, with multiple elongated filopodia and lamellipodia. Cell growth on the surface of M exhibited elongated, clustered, and multilayered morphologies alongside extended spreading of the cytoskeleton, as shown by F-actin staining (red) (Fig. $4C_3$). The 3D reconstruction of the images showed that several cellular layers covered the agglomerated M (Fig. $4C_4$ and C_5). On TEM of bone marrow-derived mesenchymal stem cells (BMSCs) cultured with M for 14 days, mitochondria that approximated the rough endoplasmic reticulum exhibited characteristic double membranes with granule-free cristae (Fig. $4D_1$).[48] Following interaction with M, n-HA entered BMSCs cells *via* endocytosis. Intracellular n-HA accumulation was demonstrated by the appearance of electron-dense granules surrounded by the rough endoplasmic reticulum. The nanocrystals maintained a uniform rod-like morphology and EDS mapping further proved the existence of Ca/P elements in n-HA, as shown in the higher-magnification images (Fig. $4D_2$).

RUNX2 is a prominent transcription factor that regulates the expression of osteogenic marker genes and promotes bone formation. Although no significant difference in expression levels was observed among the M and control groups (Fig. 4E), normal *RUNX2* mRNA expression in M indicated that M can support the differentiation of adherent cells along the osteogenic lineage. COLI is a component of the extracellular matrix and is an intermediate osteogenesis index.[49] The effect of M on *COLI* mRNA expression was less prominent for 7 days of treatment. However, M upregulated *COLI* expression at later time points (day 14, $p < 0.05$). As an essential marker of early osteogenesis, ALP expression on day 7 showed particular improvements compared with the control group ($p < 0.05$). On day 14, ALP expression in the experimental group osteoblasts with M was slightly lower than that on day 7 but higher than that of the control group ($p < 0.01$). OCN and OPN are late-stage osteogenic markers for bone maturation and bone formation.[44] Both these markers exhibited high mRNA expression levels on day 14 ($p < 0.05$). Thus, M accelerates osteogenic differentiation at an early stage and promotes extracellular matrix formation.

3.3 Degradation and osteogenesis of M *in vivo*

3.3.1 Micro-CT of the femoral condyle. The microspheres without Van (M) were implanted into the femoral condylar bone defects in rabbits to evaluate their degradation and osteogenesis abilities *in vivo*. All the animals survived until the end of the study and no perioperative period complications were encountered. Clinical and macroscopic evaluations revealed neither necrosis nor infection before bone sample retrieval. No apparent congestion, necrosis, suppuration, or other phenomena around the bone defect were observed at each time point of M implantation (Fig. $5A_1$–E_1, bottom right). The 3D reconstruction of the femoral condyle revealed a smooth bone surface without any apparent collapse or damage (Fig. $5A_1$–E_1). At the beginning of the operation, the implanted M almost filled the entire femoral condyle defect area (Fig. $5A_1$–A_3). Bone defect reconstruction in Fig. $5B_7$–E_7 demonstrated only a small amount of bone tissue being formed throughout the study period in the control group (not injected with M) even at 8 weeks following injury onset, and this fact suggested that the femoral condyle defect was of a critical size (unable to self-heal). Conversely, bone tissue regeneration was observed in the M-treated groups with increased healing time. After 10 days, some M began to degrade and none exhibited direct contact with the surrounding bone (Fig. $5B_2$ and B_3). Although a small amount of new bone had formed, the bone mass was relatively low. After 16 days, 62.62% ± 1.94% of M was degraded (Fig. 5F) and fine trabecular-like structures were visible around M (Fig. $5C_2$ and C_3) and new trabecular bone formation had filled the bone defect area with a lot of gaps (Fig. $5C_5$). Twenty-eight days later, quantitative analysis showed that 85.21% ± 1.09% of M had degraded (Fig. 5F) and that the trabecular-like structures had become sophisticated over time

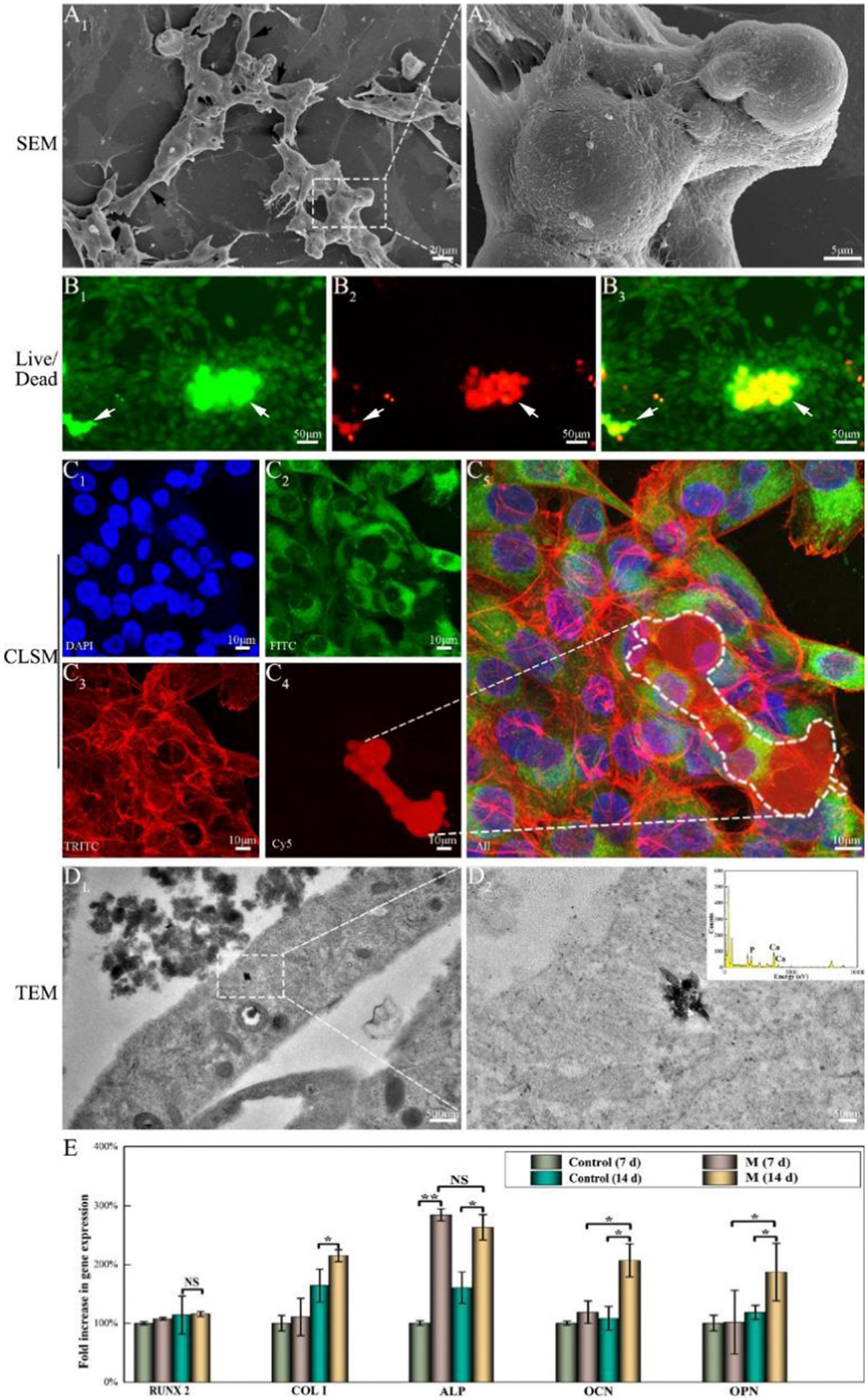

Fig. 4 Proliferation and osteogenic differentiation of cells following coculture with Gel/n-HA composite microspheres (M). SEM images (A_1) and (A_2) show MG63 cells cultured with M for 4 days (black arrow: cell bridge); fluorescence microscopy images (B_1) live cells: green; (B_2) dead cells: red and granular aggregates of M exhibit strong fluorescence) of MG63 cells cultured with M for 7 days. White arrows indicate autofluorescence of M; confocal laser scanning microscopy (C_1, blue: nucleus labeled with Hoechst dyes, ex/em ~350 nm/~461 nm); C_2, green: mitochondria labeled with MitoTracker® probes (ex/em ~490 nm/~516 nm); C_3, red: F-actin labeled with phalloidin (ex/em ~531 nm/~554 nm); C_4, red: autofluorescence of M (ex/em ~488 nm/~561 nm); C_5, merge graphs show MG63 cells cultured with M for 4 days. (D) TEM images of BMSCs cultured with M for 14 days and the EDS mapping of n-HA endocytosed by BMSCs; (E) Quantitative gene expression of BMSCs cultured in M after 7 and 14 days *via* real-time polymerase chain reaction: *RUNX2*, *COLI*, ALP, OCN, and OPN (n = 3, NS: not significant; *$p < 0.05$; **$p < 0.01$).

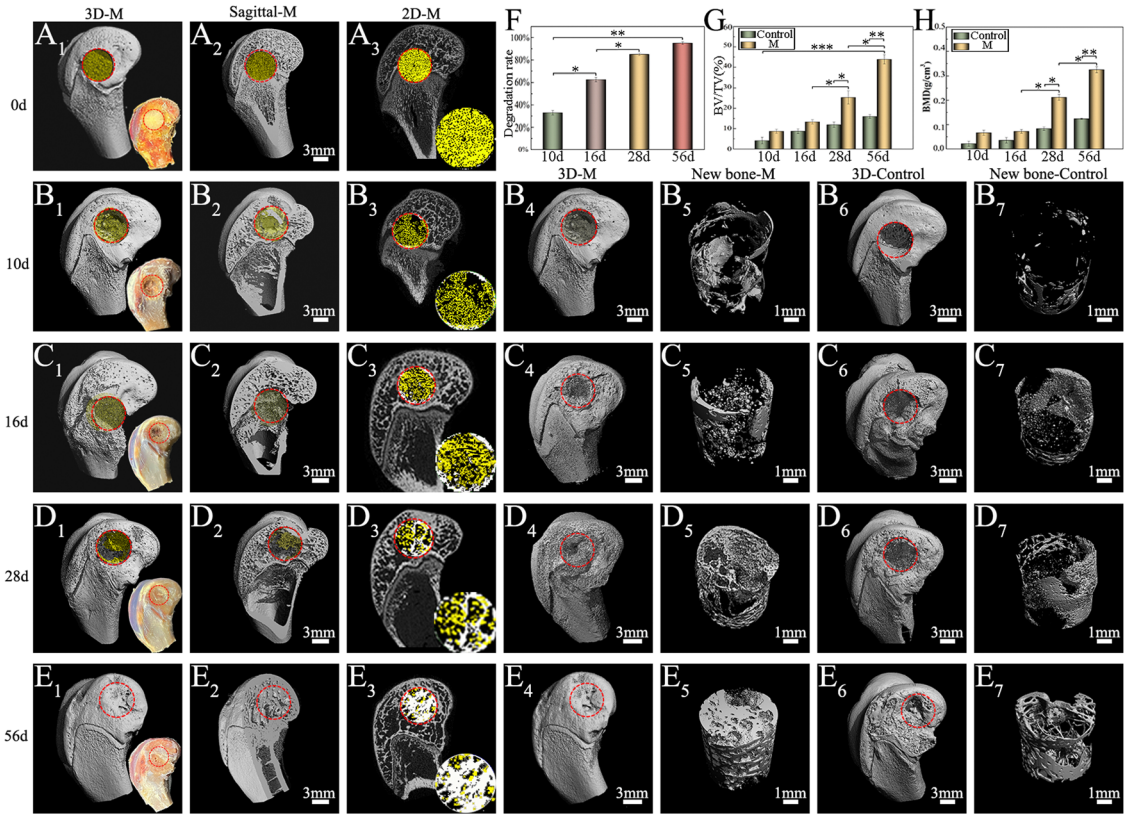

Fig. 5 Effect of injectable gelatin/nanohydroxyapatite composite microspheres (M) on bone regeneration *in vivo*. Micro-CT images of femoral condyle after M implantation at day 0 (M degradation: A_1–A_3), 10 (M degradation: B_1–B_3, osteogenesis: B_4–B_7), 16 (M degradation: C_1–C_3, osteogenesis: C_4–C_7), 28 (M degradation: D_1–D_3, osteogenesis: D_4–D_7), and 56 (M degradation: E_1–E_3, osteogenesis: E_4–E_7) (red circle: bone defect area; yellow: M; white: new bone); M degradation rate (F) and the bone volume/total volume (BV/TV) (G), bone mineral density (BMD) results of bone defect (H) *in vivo via* Micro-CT analysis (n = 3, *$p < 0.05$, **$p < 0.01$, ***$p < 0.001$).

(Fig. 5D_2 and D_3). Although the M group exhibited a large area filled with new bone, a large gap remained (Fig. 5D_5). By the 8th week, the M group showed a large amount of high-density bone (Fig. 5E_2) where the partially residual M (~5.45%) were directly integrated with the bone trabeculae (Fig. 5E_3). The BMD results showed that the M group produced a high BMD at the 8th week (Fig. 5H). The newly formed bone tissue was thicker with almost no space between the trabecular bone, and the new bone tissue was dense (Fig. 5E_5). Quantitative and BV/TV analysis confirmed the previous results (Fig. 5G).

3.3.2 Histological evaluation of femoral condyle. H&E and Masson's staining was conducted for the histological analysis of the repair acceleration efficacy of M. At 10 and 16 days, the contours of the incompletely degraded M (blue arrow) and an abundance of osteoblasts (red arrow) were observed in the M group, along with small, sparse blue collagen fibers (Fig. 6B_4 and D_4). The osteoblasts were recruited and surrounded by microspheres. In the control group, a large number of inflammatory cells around the bone defect were observed (Fig. 6A_2 and C_2). On day 28, abundant deep-stained collagen fibers were detected in the bone matrix alongside some red weaves in M; the yellow arrows point to the integration of the new bone tissue and M. These findings proved the formation of new bone (Fig. 6F_4). Conversely, the control group, without injected M as support, demonstrated only a small amount of bone tissue formation and still presented a bare cavity following the procedure (Fig. 6E_4). At the 8th week following surgery, only sparse new bone tissue formed with minimum increase around the defect in the control group (Fig. 6G_4). However, newly formed bones were clearly visible in the M group that even covered the central region of the defects (Fig. 6H_4).

3.4 Antibacterial effect of the VM

3.4.1 VM cultured with bacteria *in vitro*. The control (normal) *S. aureus* remained intact, retaining its smooth surface and typical spherical shape (Fig. 7A). *S. aureus* treated with M without Van presented an intact and smooth cell membrane without deformation (Fig. 7B_1). The damage caused directly by M to bacteria was negligible because of the good adherence of bacteria on the surface of M (Fig. 7B_2). Conversely, several holes and lesions in the bacterial cell walls/membranes appeared following VM treatment (Fig. 7C_1). More importantly, the bacterial cell wall demonstrated severe destruction, causing cytoplasmic outflow (orange arrows) (Fig. 7C_2). Nevertheless, some well-shaped bacteria remained in the VM group (blue arrows) (Fig. 7C_2). The ultrastructure of the control *S. aureus* remained intact, with a smooth cell membrane and the dense

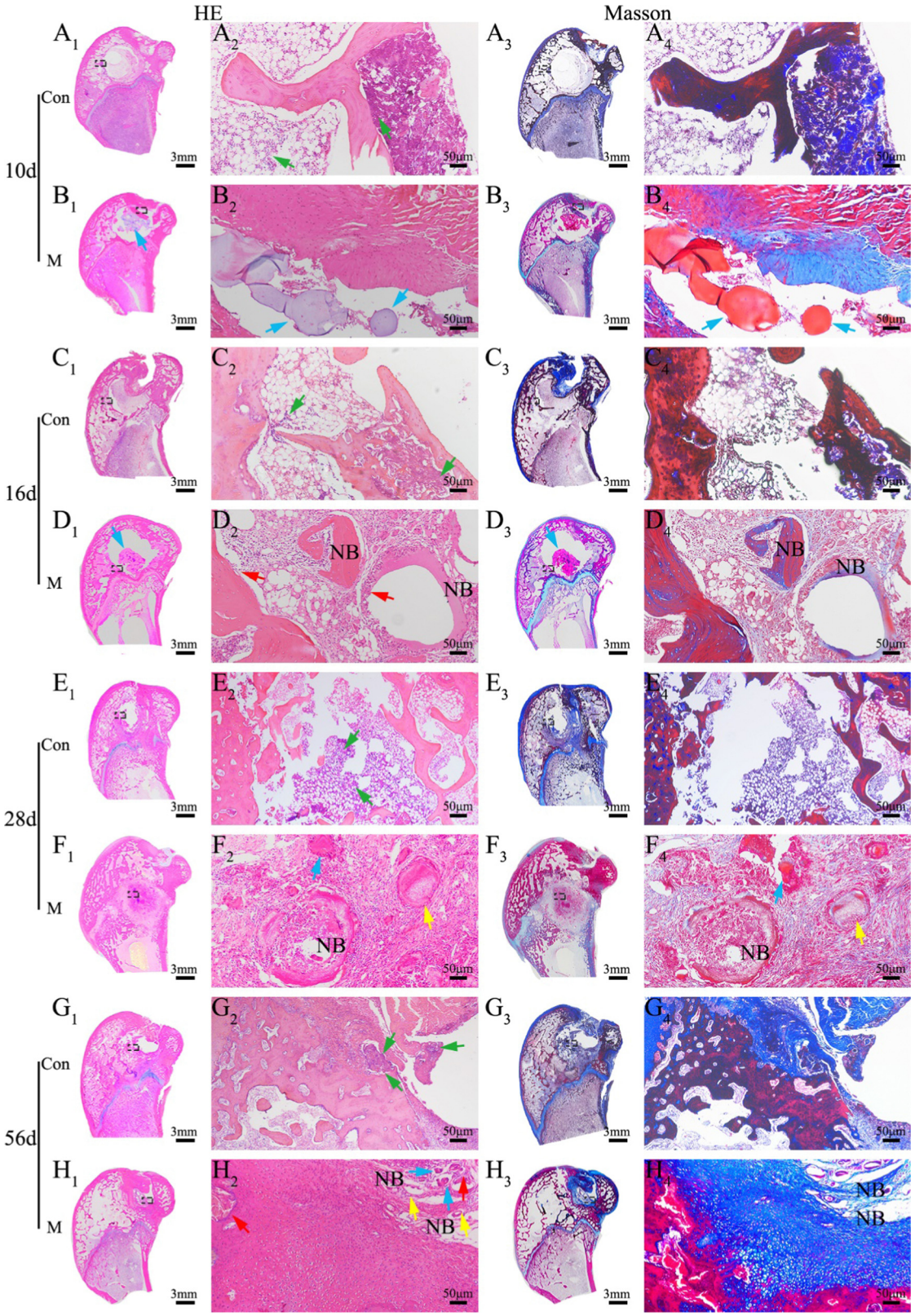

Fig. 6 Hematoxylin and eosin (H&E) and Masson's staining images of femoral condyle following gelatin/nanohydroxyapatite microsphere (M) implantation *in vivo* at day 10 (control: A_1–A_4, M: B_1–B_4); 16 (control: C_1–C_4, M: D_1–D_4); 28 (control: E_1–E_4, M: F_1–F_4); 56 (control: G_1–G_4, M: H_1–H_4). Blue arrow: M; red arrow: osteoblasts; yellow arrow: trabecular; green arrow: inflammatory cells; NB: new bone.

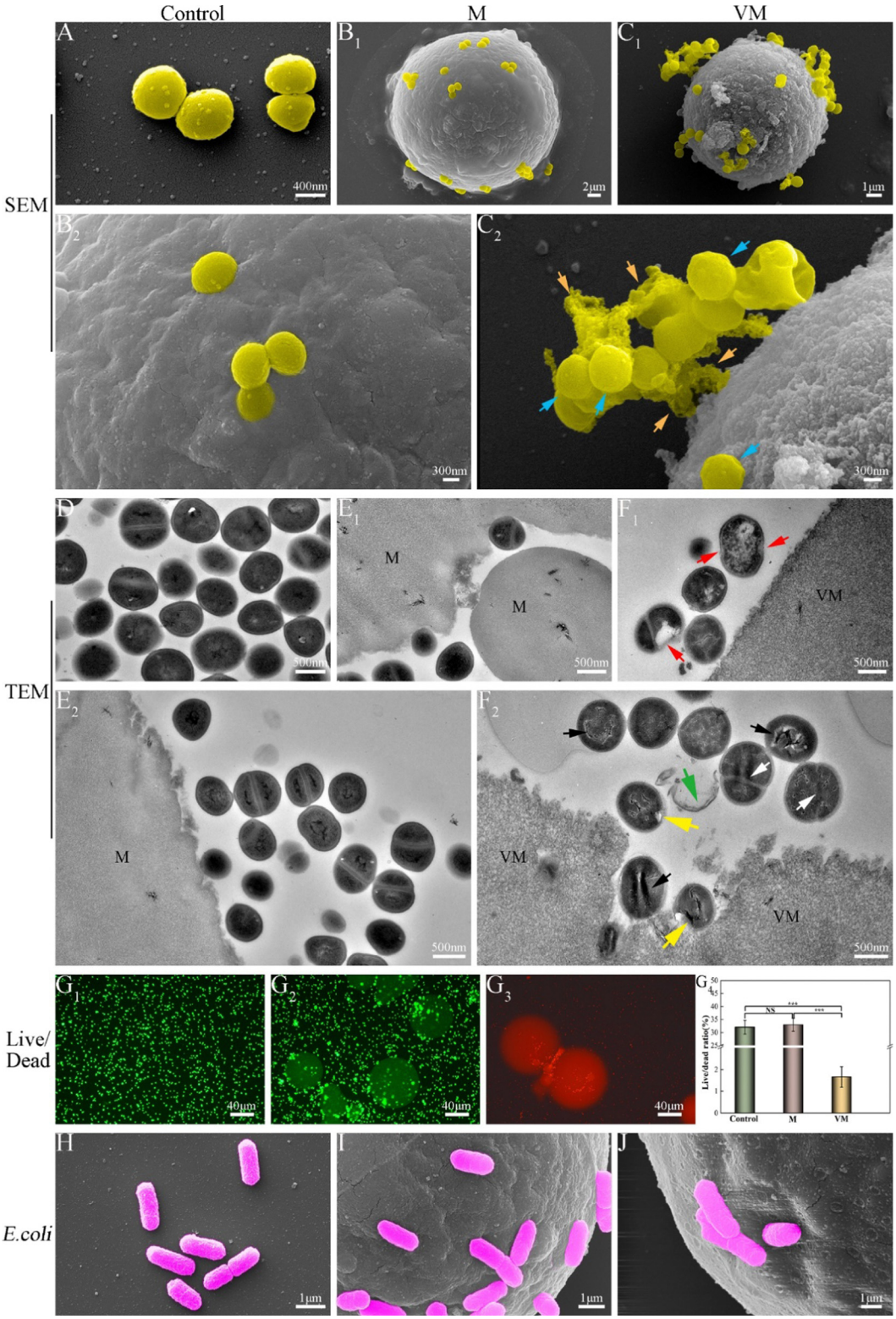

Fig. 7 Bactericidal activity of vancomycin-loaded microspheres (VM) *in vitro* with *Staphylococcus aureus* (1×10^6 CFU mL^{-1}) treated with microspheres for 24 h. A–C SEM images: A, normal (pure culture media); B, M; C, VM; D–F TEM images: D, normal; E, M; F, VM. Live/dead staining: G_1, normal; G_2, M; G_3, VM; live cells stained positive for SYTO 9 (green), whereas dead cells were visualized *via* PI staining (red). G_4: SYTO-stained live bacteria were counted using ImageJ software and expressed as the percentages of total cells. *Escherichia coli* (1×10^6 CFU mL^{-1}) treated with VM for 24 h: H, normal; I, M; J, VM. Arrows: orange: leaked cytoplasm; blue: normal bacteria; red: clear holes; black: unevenly distributed cytoplasm; yellow: damaged cell wall; white: abnormal division; green: deformed cell membrane.

and homogeneous cytoplasm; several bacteria exhibited septa forming in the middle of the cell and underwent division with an intact cell wall (Fig. 7D). As illustrated in Fig. 7E and F, *S. aureus* treated with M presented an intact and smooth cell membrane while *S. aureus* treated with VM exhibited damaged cell walls. Holes were visible in the bacteria and the cytoplasm appeared empty (red arrow) (Fig. $7F_1$), which may be due to the leakage of the cytoplasmic substrate from the broken cell envelope. In addition, although several bacteria had maintained a spherical structure, their internal cytoplasm was unevenly distributed (black arrow) (Fig. $7F_2$), and the cell wall structure was unstable, resulting in the leakage of cell contents (yellow arrow) (Fig. $7F_2$). In addition, the septal cell wall of partially divided *S. aureus* cells altered to a less clearly defined state (white arrow). Several wrinkled and deformed cell membranes were also present (green arrow) (Fig. $7F_2$). All live bacteria were stained with SYTO-9 and fluoresced green, whereas the dead bacteria labeled with PI fluoresced red.[50] Compared with the green fluorescence observed in the normal (Fig. $7G_1$) and M (Fig. $7G_2$) cells, the fluorescence of all bacteria in the VM group was red (Fig. $7G_3$). Green and red fluorescence was simultaneously present in the M- and VM-treated groups due to the strong green and red fluorescence of gelatin. Further analysis showed that the number of live bacteria decreased from 30% (M group) to 1.6% (VM group) (Fig. $7G_4$). To verify the specific antibacterial property of Van with *S. aureus*, we also cultured *Escherichia coli* with microspheres for 24 h and found that *E. coli* continued to grow normally and showed morphological integrity in the normal, M without Van, and VM groups (Fig. 7H–J, respectively).

3.4.2 Drug release behavior and antibacterial activity of VM *in vitro*. According to UV spectrophotometry, the antibiotic content and encapsulation efficiency of VM were 31.02% ± 0.86% and 96.95% ± 1.24%, respectively. Its effective drug loading and encapsulation made it simple for further drug release studies. The *in vitro* release profile of VM was monitored in phosphate-buffered saline at pH 6.0 and 7.4 for 14 days (Fig. 8A). The Van release behavior of VM at pH 6.0 was similar to the behavior of VM at 7.4, and VM showed an initial burst on the 1st day (41.00% ± 1.93%, pH 6.0; 37.29% ± 2.15%, pH 7.4), followed by sustained release. Notably, the release rate of Van from all the samples at pH 6.0 was slower than that at pH 7.4 in the initial 30 min. The amount of cumulative release increased following a parabolic curve within 4 days to ~66.02% ± 1.73% (pH 6.0) and 56.14% ± 2.40% (pH 7.4). Following this, the release rate gradually decreased, and the cumulative release was ~77.95% (pH 6.0) and ~66.32% (pH 7.4) at 14 days. However, the samples immersed in acidic solution exhibited higher release kinetics than those at pH 7.4. At pH 7.4 and 6.0, M swelled rapidly within 15 minutes and reached equilibrium after 24 h of immersion with similar trends. M in a more acidic environment (pH 6) exhibited a higher equilibrium swelling ratio than that in a neutral pH environment (pH 7.4) (Fig. 8B).

The released Van can produce visible bacterial inhibition rings after 14 days of release at both pH values, which further proved its high biological activity (Fig. 8C and D). The diameter of the formed inhibition ring gradually increased on the first day and then eventually decreased. The largest diameters of the zones were 18 mm (pH 6.0) and 15 mm (pH 7.4) at 24 h in the agar plates; thus, the rapid release of Van can produce an initially rapid period of bacterial death. After a longer release time (14 days), the diameters of the inhibition rings were only 8 mm (pH 6.0) and 7 mm (pH 7.4), although VM still maintained antibacterial activity. The bioactivity of Van at both pH values was similar within the 14 day period. However, the antibacterial effect of Van at pH 6.0 sharply increased and was more effective than that of Van at pH 7.4 within 14 days of release (except for the first 30 min).

3.4.3 Antibacterial activity evaluation of VM *in vivo*. The rabbit back muscle *S. aureus* infection model was applied to evaluate the antibacterial ability of Van-loaded microspheres (VM) *in vivo* as shown in Fig. 9. After 4 days of treatment, the bacteria were separated from the infected wound and spread on agar broth plates to culture for 24 h. No bacterial growth was observed in the culture plate of the control group (Fig. $9A_1$), thereby confirming the sterility of the operation. As coagulation factors attract neutrophils and monocytes to the wound during the wound-healing process,[51] a small number of inflammatory cells appeared on day 4 in the control group (Fig. $9C_1$). Multiple bacterial cells were observed in the blank (Fig. $9A_2$) and microspheres without Van(M) treatment groups (Fig. $9A_4$), indicating high bacterial growth in the infected tissue. In the infected muscle (Fig. $9A_2$), yellow pus and exudates were observed at the wound site. No pus was observed in the wound treated with M (Fig. $9A_4$); however, inflammation was still present. Large numbers of inflammatory cells were observed in the blank (Fig. $9C_2$) and M (Fig. $9C_4$) groups, indicating that serious inflammation remained uncontrolled owing to the absence of antibacterial activity of the treatments. Most bacteria were killed following treatment with Van (Fig. $9A_3$) or VM (Fig. $9A_5$). Moreover, the surfaces of the VM-treated wounds (Fig. $9A_5$) were moist, bright, and devoid of inflammation and the muscle defects were filled with fibrous connective tissue. Only a mild inflammatory response appeared in the wound tissues of the muscle treated with Van (Fig. $9C_3$), which was attributed to the highly effective antibiotic action of Van against *S. aureus*. The infected muscle tissue with VM treatment (Fig. $9C_5$) appeared to contain a large number of fibroblasts, scattered macrophage infiltration, and a small proportion of neutrophils. Clear granulation tissue was particularly apparent around the VM samples. Thus, these results illustrated the excellent antibacterial activity of VM *in vivo*.

3.5 Treatment of osteomyelitis *in vivo*

By the 8th week, the infected rabbit exhibited distorted periosteum and progressive cortical bone destruction (Fig. $10A_1$); purulent material at the modeling medullary cavity site can be observed in the sagittal photo (Fig. $10A_2$). MicroCT images revealed that the control group had almost no new bone formation in the defect site. Typical osteomyelitis manifestations, including severe trabecular

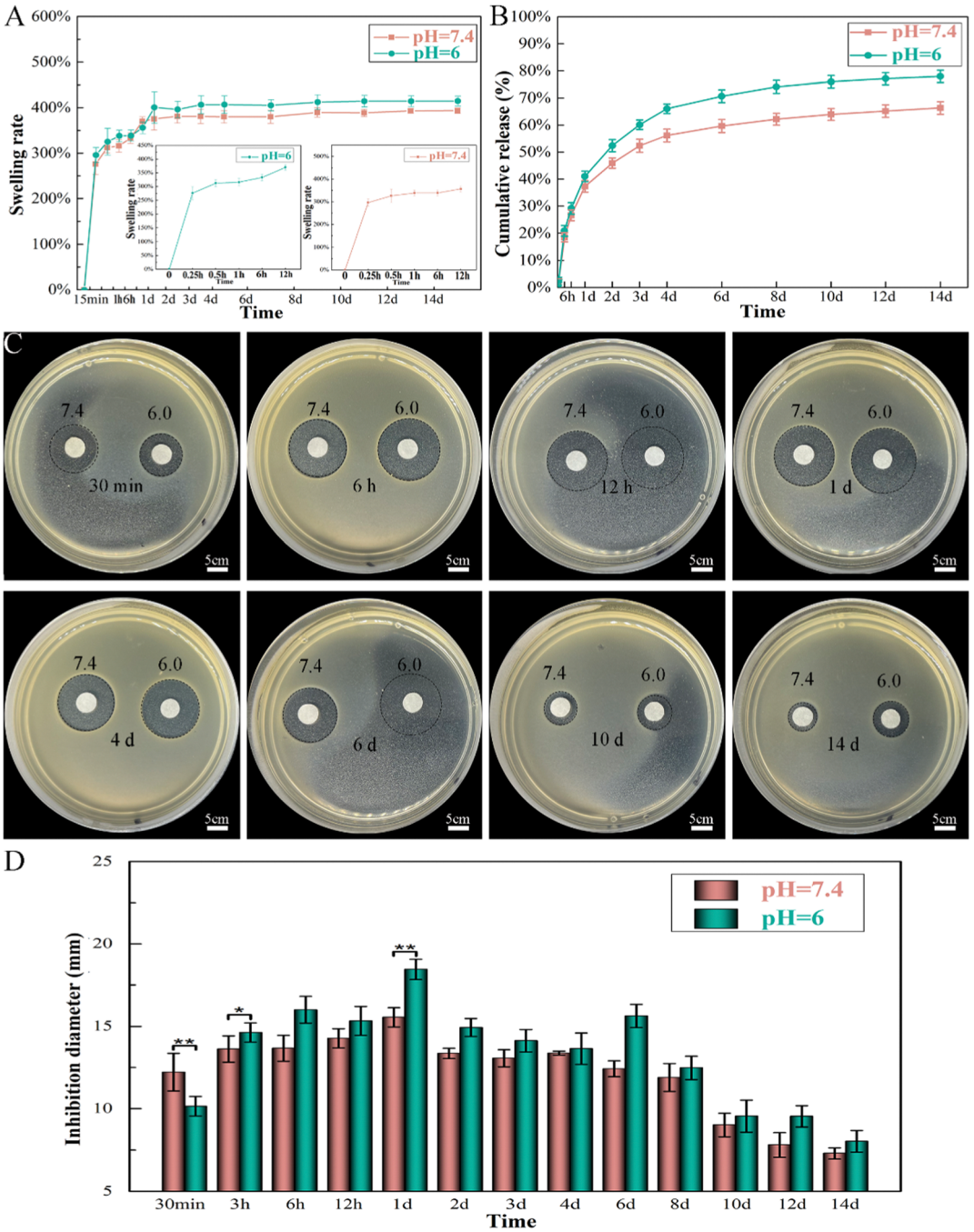

Fig. 8 Drug release and inhibition rings of vancomycin (Van)-loaded microspheres (VM) *in vitro*. (A) Van antibiotic cumulative release rate from VM at pH 6.0 and 7.4; (B) swelling behaviors of M at pH 7.4 and 6.0; (C) inhibition rings and (D) diameter of Van released from VM against *Staphylococcus aureus* at pH 6.0 and 7.4. ($n = 3$, $^{*}p < 0.05$, $^{**}p < 0.01$).

disorder (Fig. $10A_3$), osteoporosis (Fig. $10A_4$), and osteolysis (Fig. $10A_5$), were observed. In the VM group, the bone cortex was smooth and intact (Fig. $10B_1$) without swelling or ulceration (Fig. $10B_2$). CT analysis showed that the VM group exhibited good bone repair with almost complete healing of the bone defect, including the cortical bone (Fig. $10B_3$). In addition, the shape of the radiopacity area in the intramedullary bone (Fig. $10B_4$) was similar to that of the original compact bone, *i.e.*, the bone tissue was dense (Fig. $10B_5$). BV/TV and BMD (quantitative analyses of the microCT images) exhibited similar trends (Fig. 10G) where the VM group (BV/TV: 32.24%; BMD: 0.45 g/cm^3) was significantly different ($p < 0.01$) from the control group (BV/TV: 5.23%; BMD: 0.12 g cm^{-3}). Severe cortical bone destruction and fracture were observed in the control group *via* H&E staining (Fig. 10C). Conversely, in the VM group, instead of further bone destruction, regenerated cortical bone was observed at the infection site (Fig. 10D). Subsequently, sequential fluorescent labeling was used to observe new bone formation by applying two types of

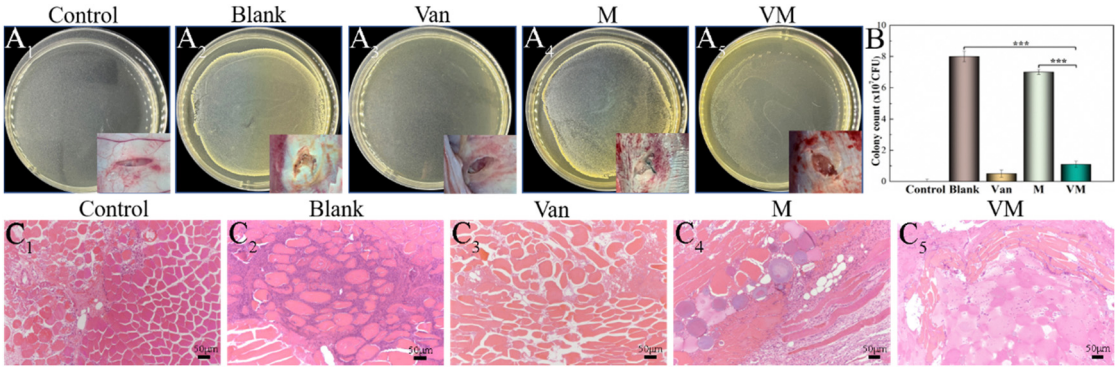

Fig. 9 Anti-inflammation of rabbit back muscles *in vivo*. (A) Representative photos of *Staphylococcus aureus* colonies on agar broth plates separated from infected wounds with different treatments on day 4 (bottom right: photocapture of rabbit muscle repair under different treatments on day 4). (B) The colony count of *S. aureus* from the different groups. (C) HE-stained images at 4 days of treatment.

fluorochromes: alizarin red (red) and calcein (green). As fluorochromes can bind to calcium ions of the newly formed bone and incorporate into the mineralization area, the new bone formed at different periods can be discriminated using different fluorochrome colors.[53] The new bone tissue was thin, and the fluorescence intensity was low in the control group after 8 weeks (Fig. 10E). In the VM group, the fluorescence images showed the complete outline of M that had not completely degraded together with new bone tissue around these M (Fig. 10F, white arrow). Strong fluorescence intensity (Fig. 10H) and dense bone tissue indicated a strong bone regeneration capability induced by treatment with VM.

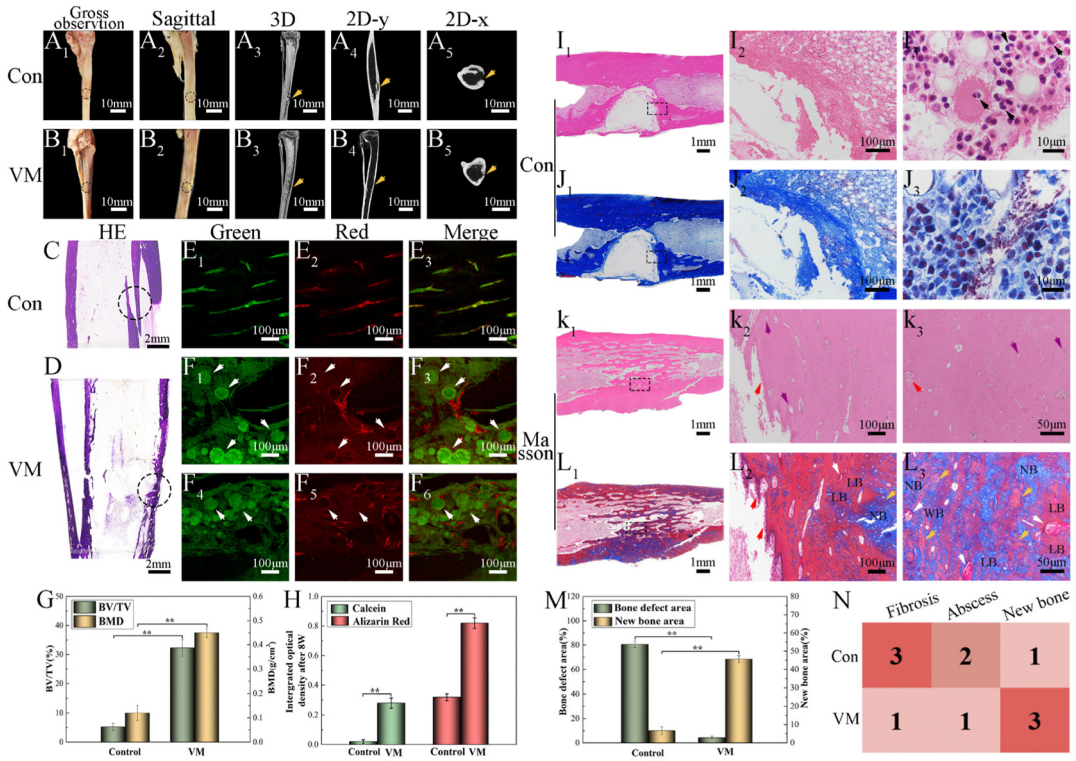

Fig. 10 *In vivo* treatment of osteomyelitis after 8 weeks. Gross observation photos and Micro-CT 3D reconstruction: (A) control; (B) VMs. Hematoxylin and eosin (H&E) staining of newly formed bone tissue: (C) control; (D) VMs. Fluorescent staining of newly formed bone tissue: (E) control; (F) VMs. Green: calcein, red: alizarin red. Black circle: bone defect; yellow arrow: modeling area; white arrow: microspheres. The bone volume/total volume and bone mineral density results of the defect area of bone modeling (G) *in vivo via* Micro-CT analysis. Summary of fluorescent labeling (H). Histological analysis of newly formed bone tissue: (I) H&E staining of the control group; (J) Masson staining of the control group; (K) H&E staining of the VM group; (L) Masson staining of the VM group. Black arrow: inflammatory cells, white arrow: microspheres, red arrow: osteoblasts, yellow arrow: trabecular, purple arrow: blood vessels, NB: new bone, LB: lamellar bone, WB: woven bone. (M) The percentage of trabecular bone area in the different treatment groups after 8 weeks; (N) for the semiquantitative assessment of the severity of infection and lack of tissue integration,[52] histological scores were determined based on the histological sections J and L (1: few; 2: moderate/focal; 3: numerous and diffuse). $n = 3$, $^{**}p < 0.01$.

The H&E staining showed that bone destruction (Fig. 10I_1) was present at 8 weeks. A severe inflammatory (Fig. 10I_2) response was observed in the control group, including dead bone, large accumulation of lymphocytes and monocytes, and neutrophil infiltration into the bone tissues. The bone defect area reached 80.56% ± 2.78% (Fig. 10M). Noticeably, neutrophils were in evidence (Fig. 10I_3, black arrow), possibly as a result of the ongoing and severe bacterial infection. Bone defects were displayed *via* the blue-stained collagen fibrous tissues using Masson's staining (Fig. 10J_1, J_2). In the VM group, bone infection was considerably suppressed (Fig. 10K_1) and the defect was completely reconstructed (Fig. 10L_1) at 8 weeks (new bone remodeling area reached 45.65% ± 1.9%) (Fig. 10M). A substantial number of new blood vessels had formed (Fig. 10K_2, K_3, purple arrow). Several new blood vessels were present around the newly formed trabeculae (yellow arrow) aligned by osteoblasts (red arrow), suggesting active bone formation. Osteocytes and the lamellar features of the newly synthesized bone around M (white arrow) indicated bone maturation. A thick layer of randomly oriented woven bone was gradually translated into compact and stress-oriented lamellar bone (Fig. 10L_2, L_3). The histological scores (Fig. 10N) demonstrated that VM exhibited the ability to eliminate existing infections and guide bone tissue regeneration.

4. Discussion

The clinical treatment of osteomyelitis usually includes surgical debridement, necrotic bone removal, and subsequent biomaterial transplantation to fill the void. It is critical to develop new therapeutic strategies for antibiotic delivery with sustained release characteristics alongside high bioactivity that can neutralize the negative effects of high local antibiotic concentrations.[54] Here, we have developed an antibiotic delivery microcarrier consisting of Gel/n-HA microspheres loaded with Van that simultaneously exhibits an improved ability to induce cell recruitment and targeted antimicrobial characteristics for effective osteomyelitis treatment.

4.1 Preparation and sustained drug release of Van-loaded Gel/n-HA microspheres

Topical delivery systems tend to exhibit suboptimal release characteristics that produce antibiotic concentrations that are thousand times higher than those required to inhibit bacterial growth.[55] Synthetic conditions and crosslinking of Gel microspheres considerably affect drug release from M by impacting the particle size and drug distribution The sizes of Gel microspheres formed *via* chemical crosslinking using the water-in-oil emulsion method can be adjusted from 10 to 400 μm by tuning the preparation conditions, such as the viscosity of the Gel solution, type and concentration of organic solvent and surfactant and oil, and the stirring speed.[56,57] The conditions applied here synthesized Gel microspheres in the size range of 8.7–51.8 μm (Fig. 3A). The smooth surface of M indicated a tight surface structure (Fig. 3B). In the composite formation stage, the COOH groups of Gel exist as COO^- ions and electrostatically bind with the Ca^{2+} ions of n-HA,[58] and this process produced a slight shift of P (Fig. 3C). The water-soluble zero-length crosslinker, EDC, promoted the formation of amide bonds between the carboxyl and amino groups ($-NH_2$) of Gel and but was not incorporated into the crosslinked structure (Fig. 3E), which is preferable for crosslinking Gel microsphere carriers.[59] After EDC crosslinking, changes in the amide bonds of M occurred because of the enhanced interaction of the amide functional groups in the Gel (Fig. 3C). The formation of small porous structures (Fig. 3B) on the surface of M resulted from the dispersion of n-HA in M or phase separation due to the exchange of water solvent and acetone (nonsolvent) during the polymer solution precipitation process.[60] The strategy of incorporating antimicrobials into biomaterials was achieved *via* physisorption in this study by immersing the substrate in the antimicrobial-containing solution. The infrared spectrum of VM (Fig. 3C) revealed that Van did not react with Gel and n-HA. n-HA particles exhibit greater solubility, higher surface energy, and stronger adsorption.[61] By adding positively charged Van, n-HA, which can bind with neutral, positively charged, and negatively charged molecules, adsorbed more Van and formed more pores (Fig. 3B) in the inner structure. These interior pores facilitate water uptake from the media, providing diffusion channels for drugs.

The release kinetics of Van at pH 6.0 and 7.4 were analyzed by fitting the cumulative release data (solid line) to an exponential equation (dashed line) as shown in Fig. 11A. The fitted equations of Van release before 60% were $M_t/M_\infty = 0.1218 \times (t - 0.5)\ 0.5646 + 0.0692$ ($r^2 = 0.9774$) (pH 6.0) (Fig. 11A_1) and $M_t/M_\infty = 0.0894 \times (t - 0.5)\ 0.5395 + 0.0915$ ($r^2 = 0.9669$) (pH 7.4) (Fig. 11A_2). As both release exponents were between 0.43 and 0.85, their release mechanism was the superposition of Fickian diffusion and Case-II transport.[62] The simple adsorption of Van on the surface of microspheres created a relatively fast burst release at pH 6.0 and 7.4 that occurred *via* diffusion.[63] The presence of bacteria lowers the environmental pH value (pH < 6.5) due to the release of lactic or acetic acid. The isoelectric point (pI) of Van is ~8.30, and the compound is positively charged in an acidic solution.[64] The repulsive forces between the positive charges of Van and high protonation in acidic solution could limit the release rate of Van at pH 6.0; thus, the release rate at pH 7.4 was higher in the first 30 min. The swelling property is essential for microspheres in tissue engineering, and most microspheres, especially those with a large amount of amino groups (such as Gel), will swell in an aqueous solution, resulting in Gel expansion.[65] Here, microspheres swelled rapidly in aqueous solution within 15 min (Fig. 6B). The crosslinking of Gel with EDC can form a large number of amide bond-crosslinking networks (Fig. 11B-II). However, amide bonds are sensitive to H^+ in the acidic phosphate-buffered saline (Fig. 11B-IV). The breaking of amide bonds under acidic conditions facilitates the penetration of water molecules into the Gel network structure, yielding both a shortened swelling equilibrium time and an enhanced equilibrium swelling ratio.[66] With the increase in the volume of

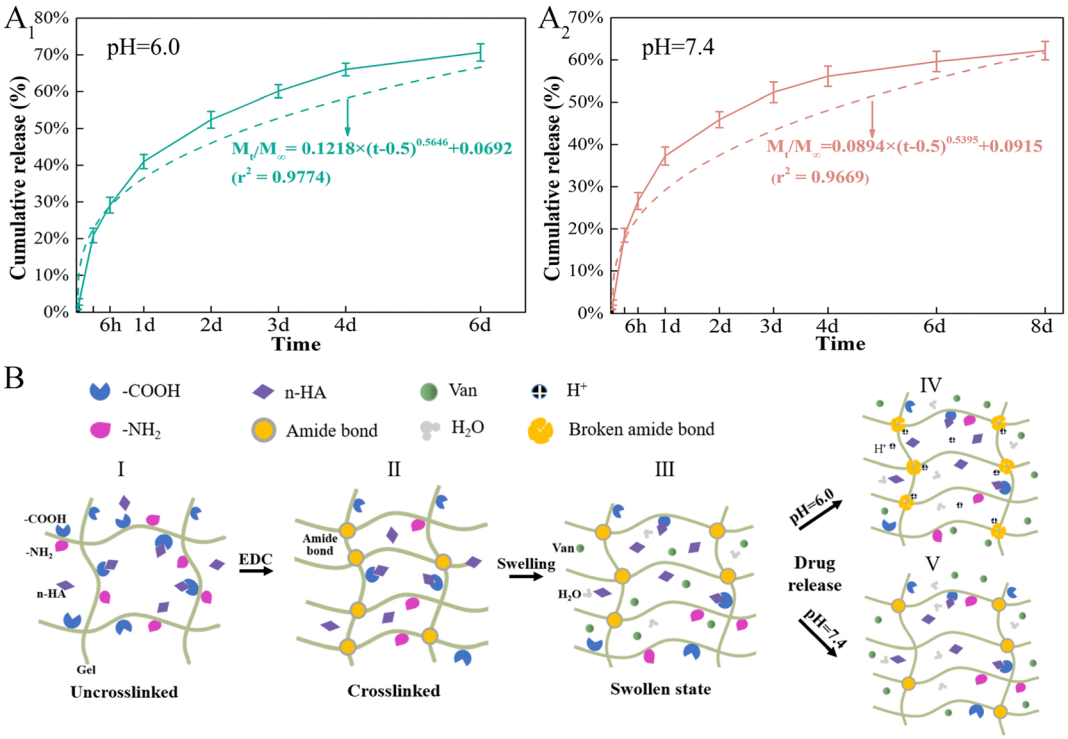

Fig. 11 Van release mechanism from Van-loaded microspheres (VM). (A) Release kinetics of Van from VM in different pH environments, (B) Schematic diagram of pH-responsive release behavior of VM.

absorbed water, the mobility of Gel macromolecules and the free volume available for diffusion increase, which further facilitates buffer penetration and high drug release.[67] At low pH, Van exhibited a higher release rate from VM than normal, which will benefit the delivery system for treating infections associated with localized acidity.

4.2 Targeted antibacterial effect of Van-loaded Gel/n-HA microspheres

As elaborated in Section 3.4.2, the as-prepared Van-loaded Gel/n-HA microspheres (VM) exhibit continuous drug release and effective antibacterial activity against *S. aureus* (Gram-positive). Following VM treatment, the cell membranes of some *S. aureus* were disrupted, causing cytoplasm leakage (Fig. 7C). Ultrastructural analysis revealed that the internal structure of bacteria treated with VM had altered (Fig. 7F_1 and F_2). Live/dead staining difference in Fig. 7G further confirmed that these bacteria had died. Gram-positive bacteria, which have peptidoglycan precursors on the surface of their cytoplasmic membrane (Fig. 12A), and Van, which can form an intricate network of hydrogen bonds with the D-Ala–D-Ala region of lipid II in *S. aureus*, will interfere with the maturation process of the peptidoglycan layer.[68,69] This will further weaken the cell wall of the bacteria, and render the cells susceptible to lysis due to alterations in osmotic pressure.[70] Gram-negative bacteria, such as *E. coli*, are protected by the outer lipopolysaccharide membrane that is impermeable to large biomolecules, such as Van, and hydrophobic compounds from the environment (Fig. 12B).[71] Therefore, Van released from VM cannot form an intricate network of hydrogen bonds with the D-Ala–D-Ala region to kill *E. coli* (Fig. 12B), as confirmed by SEM images (Fig. 7), indicating the inefficiency of VMs against *E. coli*. In the rabbit traumatic infection model, the pure Van group exhibited rapid killing of bacteria at the infected site in a short time, but the infection may return after 1–3 days. The sustained and targeted drug release from inside the VM particle after absorbing water demonstrates the sustained antibacterial activity of VM.

4.3 Cell recruitment and osteoblast activity of Gel/n-HA microspheres

The survival of anchorage-dependent cells, such as MG63 and BMSCs, initially depends on the successful ligation between cell surface receptors and specific protein domains on substrates. As a denatured collagen product, Gel contains bioactive sequences that can be recognized and integrated by integrins, such as RGD peptides.[72] As expected, SEM (Fig. 4A) and CLSM (Fig. 4C) showed the rapid recruitment and attachment of MG63 cells on the surface of M. Unlike other chemical crosslinked Gel microspheres, the cell-friendliness of the EDC crosslinker avoids the potential cytotoxicity of conventional chemical crosslinkers, such as glutaraldehyde,[73] and thus supports cell survival and growth better (as shown by live/dead staining, Fig. 4B). This triggers the focal adhesion and cytoskeletal organization of successfully recruited cells, which in turn induces cell spreading and regulates numerous other cellular behaviors, such as proliferation and differentiation.[74] Granules normally gain intracellular access *via* one of three pathways:

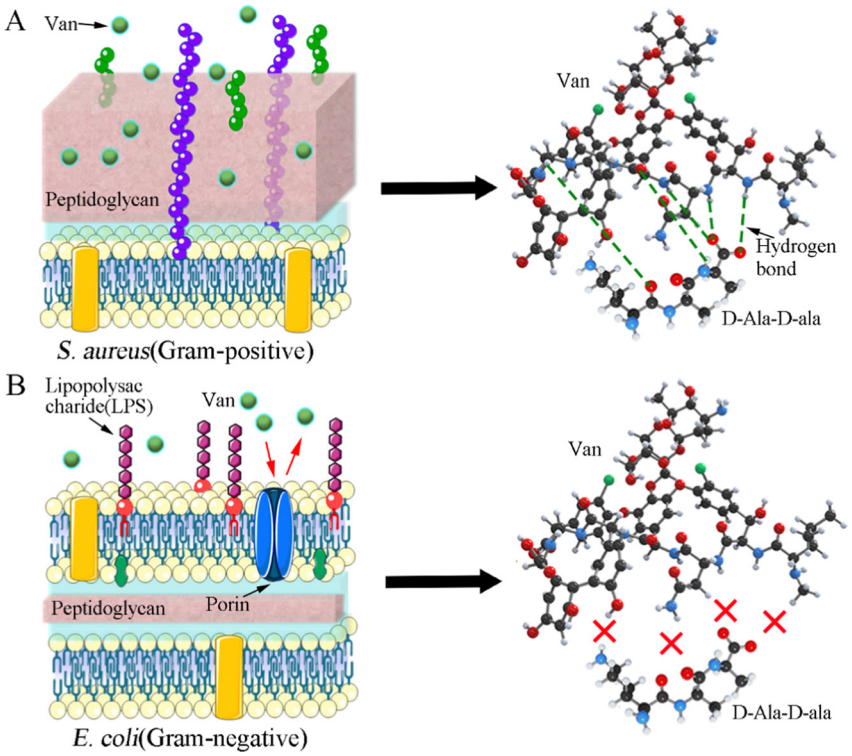

Fig. 12 Antibacterial mechanism of Van against two bacteria. (A) *Staphylococcus aureus*; (B) *Escherichia coli*.

pinocytosis, receptor-mediated pinocytotic process, and ''swallowing.'' Owing to the higher phase activity of n-HA, it was easy to enter cells *via* ''swallowing''.[44] TEM images (Fig. 4D) showed a close interaction of n-HA released from M with cells, followed by an internalization process *via* endocytosis pathways. n-HA can promote osteogenesis *via* the WNT/β-catenin pathway, favoring the induction of osteogenic transcription factor expression[75] (Fig. 13). Treatment with M caused a significant increase in the mRNA expression of the osteoblastic markers ALP, OCN, OPN, and *COLI* (Fig. 4E). In summary, the significant increase in the mRNA expression of these osteogenesis-related genes suggests enhanced ossification of BMSCs cocultured in M. The random accumulation of M can maintain a 3D configuration that can fill a void (Micro-CT results; Fig. 5) and guide the migration and growth of tissues.[76] The pore channels built between M were reported to play a critical role in accelerating bone recovery.[77] Here, M can provide important physical support within the empty bone space, which can prevent secondary fracture and modulate and accelerate osteoinduction, and by this means the formation and thickening of new bone tissue were facilitated. By the 8th week, the microspheres of the treatment groups were nearly all degraded, even though a large amount of mature bone was growing from the Gel residue. Osteogenesis tended to occur at the microsphere locations in addition to the periphery of the defective areas. The degraded, uneven microspheres were directly integrated with the bone trabeculae (Fig. 6), indicating that microspheres were retained at the target site and ossified with their hierarchical micro/nanostructures, thereby demonstrating excellent osteoinduction and osseointegration abilities.[78]

4.4 Treatment of rabbit osteomyelitis

An ideal local delivery system should provide a sustained release of antibiotics against *S. aureus* (10–20-fold above the minimum inhibitory concentration) during osteomyelitis treatment.[70] Here, the Van concentration was maintained at ~50 μg mL^{-1} 14 days after VM release *in vitro* (Fig. 8A) (where the Van MIC for *S. aureus* was >2 μg mL^{-1}).[79] A rabbit model of osteomyelitis was utilized to assess the targeted antibacterial, inflammation modulatory, osteoblast recruitment, and bone regenerative properties of VM *in vivo*. The surgical debridement of osteomyelitis leaves a large void, which is caused by the removal of sequestra and resection of the scarred and infected bone and soft tissue. The void needs to be filled to prevent recurrence and bone instability after significant bone loss. Herein, with the recurrence of osteomyelitis by *S. aureus* strains (Fig. $2A_1$–A_5), debridement alone cannot effectively remove bacteria and guide bone tissue regeneration (Fig. 10A and C). The micrometer size and carrying capability of M empowered them to deliver drugs to infected sites with sustained release, which makes them a promising drug delivery system. The as-prepared Gel microspheres exhibited a good injectability (Fig. 3D) and could be injected into the bone defect through a minimally invasive surgery to fill irregular bone defects for subsequent cell adhesion, proliferation, and osteogenesis.[80] According to the osteomyelitis *in vivo* model, it was confirmed

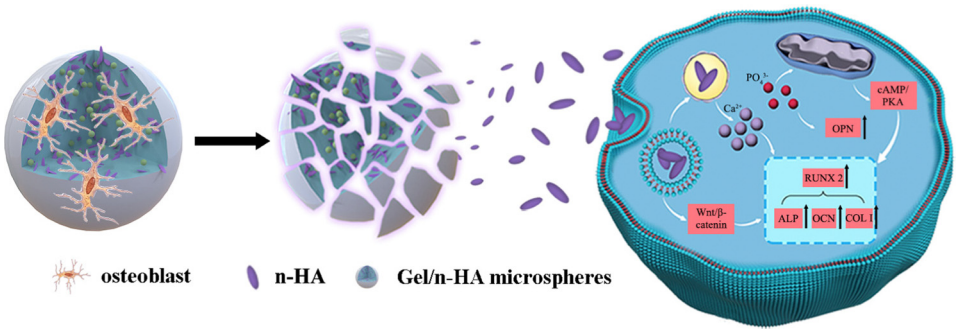

Fig. 13 Schematic diagram of osteogenic differentiation of M.

that the VM group is more effective in eliminating the existing infection than unloaded M (Fig. 10K). The sustained Ca^{2+} and P release induced by the degradation of M which can stimulate both cell proliferation and aggregation[18] is important for producing a critical cell mass required to initiate bone tissue formation. The large number of osteoblasts revealed in the H&E staining (Fig. 10K and L) assay confirmed the cell recruitment effect of M. Hence, the assembled system promotes osteogenic factor secretion and osteogenic gene expression, thereby accelerating new bone formation.

5. Conclusions

In this study, an effective drug release system and experimental model based on injectable Gel/n-HA composite microspheres (M) for treating severe osteomyelitis caused by *S. aureus* was designed and fabricated. Specifically, Van was loaded in the M (VM) to ensure the sustained release of the drug from VM for an extended period to support bone tissue regeneration without inflammation. *In vitro* and *in vivo* experiments indicated that the VM could specifically target *S. aureus* and demonstrated its efficient localized antibacterial activities in a rabbit back muscle model. In summary, our injectable VM exhibited a successful treatment outcome *via* targeted antibacterial, inflammation modulatory, osteoblast recruitment, and bone regenerative properties to treat osteomyelitis. In the future, our research will focus on infection and anti-infection, and examine the angiogenesis mechanism of VM in a controlled delivery system for osteomyelitis treatment.

Author contributions

Rui Zhang: conceptualization, methodology, investigation, writing—original draft, and writing—review and editing. Li Chen: resources investigation and project administration. Yijing Stehle: resources investigation and project administration. Mingyue Lin: investigation and methodology. Chenxin Wang: investigation and methodology. Yufan Li: investigation and methodology. Min Huang: resources investigation and project administration. Yubao Li: conceptualization, methodology, writing—review and editing, and funding acquisition. Qin Zou: conceptualization, methodology, writing—review and editing, and funding acquisition.

Conflicts of interest

The authors declare that they have no known competing financial interests or personal relationships that could have appeared to influence the work reported in this paper.

Acknowledgements

We would like to thank Guiping Yuan, Shanling Wang, and Yi He at the Analytical &Testing Center of Sichuan University for their help with TEM and SEM analysis. This work was supported by the China NSFC project [no. 32171338], Innovation and Reform Project of Postgraduate Education of Sichuan University in 2021, Experimental Technology Research Project of Sichuan University [no. SCU221099] and Analysis and Test Technology Innovation Project of Analytical & Testing Center.

References

1 J. M. Sadowska and K. J. Genoud, *et al.*, *Mater. Today*, 2021, **46**, 136–154.
2 Y. Yang and M. Li, *et al.*, *Bioact. Mater.*, 2023, **25**, 594–614.
3 N. Kavanagh and E. J. Ryan, *et al.*, *Clin. Microbiol. Rev.*, 2018, **31**(2), e00084–17.
4 X. Qu and H. Yang, *et al.*, *Bioact. Mater.*, 2021, **6**, 4607–4624.
5 D. P. Lew and F. A. Waldvogel, *Lancet*, 2004, **364**, 369–379.
6 D. K. Mills and U. Jammalamadaka, *et al.*, *Bioact. Mater.*, 2018, **3**, 157–166.
7 S. Ghosh and S. Mukherjee, *et al.*, *Biomacromolecules*, 2022, **23**, 592–608.
8 Y. Gao and Q. Ma, *Smart Med.*, 2022, **1**(1), e20220012.
9 H. A. Durr and N. D. Leipzig, *Mater. Adv.*, 2023, **4**, 1249–1257.
10 P. F. Wei and Z. Y. Yuan, *et al.*, *Biomater. Sci.*, 2018, **7**, 272–286.
11 F. Tian and B. Chi, *et al.*, *Biomater. Sci.*, 2020, **8**, 6212–6224.
12 X. Zhao and L. Wang, *et al.*, *Biomater. Sci.*, 2020, **8**, 1702–1710.
13 L. Cai and D. Xu, *et al.*, *Eng. Regen*, 2021, **2**, 109–115.

14 T. Wu and L. Liu, *et al.*, *Biomater. Sci.*, 2023, **11**, 2877–2885.
15 A. Maihemuti and H. Zhang, *et al.*, *Bioact. Mater.*, 2023, **26**, 77–87.
16 O. Song and X. Luo, *Mater. Adv.*, 2022, **3**, 8323–8331.
17 L. Liu and W. Jia, *et al.*, *Int. J. Biol. Macromol.*, 2022, **206**, 277–287.
18 R. Zhang and M. Lin, *et al.*, *Int. J. Polym. Mater.*, 2022, 1–12.
19 F. Tao and S. Ma, *et al.*, *Carbohydr. Polym.*, 2021, **251**, 117063.
20 V. Yarlagadda and P. Sarkar, *et al.*, *Angew. Chem., Int. Ed.*, 2016, **55**, 7836–7840.
21 S. Zhang and G. Chen, *et al.*, *Mater. Sci. Eng., C*, 2022, **135**, 112681.
22 J. Chen and Y. Zhang, *et al.*, *Colloids Surf., B*, 2015, **135**, 581–587.
23 C. A. Custodio and R. L. Reis, *et al.*, *Adv. Healthcare Mater.*, 2014, **3**, 797–810.
24 Y. Yu and R. X. Wu, *et al.*, *J. Mater. Chem. B*, 2016, **4**, 569–584.
25 H. Ke and H. Yang, *et al.*, *Adv. Sci.*, 2023, **10**(3), e2204528.
26 Z. Mu and K. Chen, *et al.*, *Adv. Healthcare Mater.*, 2020, **9**, e1901469.
27 B. Cai and Q. Zou, *et al.*, *RSC Adv.*, 2016, **6**, 85735–85744.
28 M. A. Vandelli and F. Rivasi, *et al.*, *Int. J. Pharmaceut.*, 2001, **215**, 175–184.
29 Q. Zou and J. Li, *et al.*, *Int. J. Biol. Macromol.*, 2015, **79**, 736–747.
30 J. Liu and Q. Zou, *et al.*, *Mater. Design*, 2021, **210**, 110047.
31 X. Li and Q. Zou, *et al.*, *Small*, 2019, **15**, e1901617.
32 J. Baek and H. Lee, *et al.*, *ACS Biomater. Sci. Eng.*, 2018, **4**, 846–856.
33 Y. Qiao and J. He, *et al.*, *ACS Nano*, 2020, **14**, 3299–3315.
34 A. S. Ram and K. Matuszewska, *et al.*, *Front. Vet. Sci.*, 2021, **8**, 758295.
35 A. Dinache and M. Boni, *et al.*, *Colloids Surf., A*, 2015, **480**, 328–335.
36 Q. Zhang and Y. Du, *et al.*, *Carbohydr. Polym.*, 2022, **277**, 118880.
37 S. Cao and L. Li, *et al.*, *Colloids Surf., B*, 2021, **207**, 112013.
38 B. Jia and Z. Zhang, *et al.*, *Biomaterials*, 2022, **287**, 121663.
39 L. A. Poultsides and L. K. Papatheodorou, *et al.*, *J. Orthop. Res.*, 2008, **26**, 1355–1362.
40 C. W. Norden and R. L. Myerowitz, *et al.*, *Int. J. Exp. Pathol.*, 1980, **61**, 451–460.
41 X. Zhang and W. Jia, *et al.*, *Biomaterials*, 2010, **31**, 5865–5874.
42 Y. Sun and Q. Zhou, *et al.*, *Small*, 2022, **18**(36), 2201656.
43 M. Lei and X. Qu, *et al.*, *Adv. Funct. Mater.*, 2019, **29**(18), 1900065.
44 Y. Li and Y. Wang, *et al.*, *ACS Biomater. Sci. Eng.*, 2020, **6**, 320–328.
45 T. Liu and N. Dan, *et al.*, *RSC Adv.*, 2015, **5**, 34511–34516.
46 X. Yu and Q. Pan, *et al.*, *RSC Adv.*, 2018, **8**, 37424–37432.
47 H. Wang and S. C. Leeuwenburgh, *et al.*, *Tissue Eng., Part B*, 2012, **18**, 24–39.
48 D. D. Pei and J. L. Sun, *et al.*, *Adv. Sci.*, 2018, **5**, 1800873.
49 B. Jia and H. Yang, *et al.*, *Bioact. Mater.*, 2021, **6**, 1588–1604.
50 X. Qi and Y. Huang, *et al.*, *Adv. Sci.*, 2022, **9**, e2106015.
51 Z. Ming and L. Han, *et al.*, *Adv. Sci.*, 2021, **8**, e2102545.
52 J. Min and K. Y. Choi, *et al.*, *ACS Nano*, 2016, **10**, 4441–4450.
53 B. Liu and J. Li, *et al.*, *Mater. Sci. Eng., C*, 2020, **112**, 110905.
54 M. Diba and B. Pape, *et al.*, *Acta Biomater.*, 2017, **58**, 67–79.
55 S. Sankaran and J. Becker, *et al.*, *Small*, 2019, **15**, e1804717.
56 M. Nouri-Felekori and M. Khakbiz, *et al.*, *Int. J. Pharm.*, 2019, **557**, 208–220.
57 D. Zhang and W. Li, *et al.*, *Eng. Regen*, 2022, **3**, 258–261.
58 F. Wang and Y. Wen, *et al.*, *Mater. Sci. Eng., C*, 2016, **69**, 268–275.
59 A. Bigi and G. Cojazzi, *et al.*, *Biomaterials*, 2001, **22**, 763–768.
60 X. Liu and Y. Won, *et al.*, *Biomaterials*, 2006, **27**, 3980–3987.
61 X. Dong and Y. Sun, *et al.*, *Small*, 2021, **17**, e2007672.
62 P. L. Ritger and N. A. Peppas, *J. Controlled Release*, 1987, **5**, 23–36.
63 N. Kamaly and B. Yameen, *et al.*, *Chem. Rev.*, 2016, **116**, 2602–2663.
64 N. Hassani Besheli and F. Mottaghitalab, *et al.*, *ACS Appl. Mater. Interfaces*, 2017, **9**, 5128–5138.
65 G. Li and S. Liu, *et al.*, *Nat. Commun.*, 2023, **14**, 3159.
66 J. Chen and J. S. Caserto, *et al.*, *Bioact. Mater.*, 2022, **14**, 52–60.
67 Y. Xue and L. Xu, *et al.*, *J. Controlled Release*, 2023, **357**, 196–209.
68 J. Zhu and W. Chen, *et al.*, *Mater. Adv.*, 2022, **3**, 7687–7708.
69 Z. Wu and Z. Zhong, *et al.*, *Mater. Adv.*, 2022, **3**, 4295–4309.
70 B. Cao and F. Xiao, *et al.*, *Small*, 2018, **14**, e1802008.
71 S. Xiao and L. Yuan, *et al.*, *Surf. Coat Tech.*, 2023, **463**, 129525.
72 J. W. Nichol and S. T. Koshy, *et al.*, *Biomaterials*, 2010, **31**, 5536–5544.
73 J. Sun and D. Wei, *et al.*, *Biomaterials*, 2014, **35**, 4759–4768.
74 J. Jiang and A. Liu, *et al.*, *Colloids Surf., B*, 2020, **188**, 110798.
75 D. Cheng and R. Ding, *et al.*, *ACS Appl. Mater. Interfaces*, 2023, **15**, 19951–19965.
76 D. Wei and R. Qiao, *et al.*, *Small*, 2018, **14**, e1800063.
77 A. K. Kudva and A. D. Dikina, *et al.*, *Acta Biomater.*, 2019, **90**, 287–299.
78 L. Wu and Y. Xu, *et al.*, *Chem. Eng. J.*, 2022, **439**, 135692.
79 S. J. van Hal and T. P. Lodise, *et al.*, *Clin. Infect. Dis.*, 2012, **54**, 755–771.
80 P. Du and A. D. S. Da Costa, *et al.*, *Mater. Sci. Eng., C*, 2020, **113**, 110961.